

POLITECNICO DI TORINO

Master's Degree in Aerospace Engineering



Master's Degree Thesis

**Development and validation of an
Adaptive Mesh Refinement algorithm for
CFD simulations of jets in nuclear
reactors**

Supervisors

Dr. Andrea ZAPPATORE

Dr. Antonio FROIO

Candidate

Danilo CATERINO

July 2022

Summary

In the last years, modern computational fluid dynamics started to have a significant role during the design phase and safety reviews of most nuclear systems. The American Society of Mechanical Engineers (ASME) V&V 30 Subcommittee on Verification and Validation in Computational Nuclear System Thermal Fluids Behavior launched a series of problems and challenges in order to test the state of the practice in using and applying computational tools. The purpose of this Master's thesis is to provide an answer to the benchmark problem no.2: "Single-Jet Computational Fluid Dynamics (CFD) Numeric Model Validation". This thesis outlines the process of validating multiple RANS and DES setups using experimental data provided by previous 2D TR-PIV experiments. Part of this work was presented at the 33rd Parallel Computational Fluid Dynamics International Conference (ParCFD 2022). One of the main points is the implementation of the Adaptive Mesh Refinement (AMR) model and how it affects the results compared with the other setups and the experimental data.

Acknowledgements

*Computational resources provided by hpc@polito, which is a project of Academic Computing within the Department of Control and Computer Engineering at the Politecnico di Torino
(<http://hpc.polito.it>)*

Table of Contents

List of Tables	VI
List of Figures	VII
1 Introduction	1
1.1 The ASME benchmark problem no. 2	2
1.2 Facility overview	2
1.3 Experiments and available data description	4
2 Simulations' outline	7
2.1 The impinging jet problem	7
2.2 Computational domain	8
2.3 The Adaptive Mesh Refinement model	10
2.4 CFD data collection	12
3 Re5 URANS $\kappa - \epsilon$ case study	14
3.1 Mesh setups definition	14
3.2 Results	17
4 Re5 DES case study	21
4.1 Mesh changes for DES	21
4.2 DES AMR setups definition	23
4.3 Results	26
5 Error estimation	40
6 Conclusions and perspective	46
A Periodic simulation for inlet boundary conditions	48
A.1 Computational domain definition	48
A.2 Boundary physics values needed	50

B Preliminary jet oscillation study	52
Bibliography	54

List of Tables

1.1	Inlet conditions for different experimental sets.	4
1.2	Example of experimental data table for $Re_5=12819$ at $y/D = 9$. . .	6
2.1	Boundary conditions for the 3D computational domain.	10
2.2	Water physical properties used for CFD simulations.	11
2.3	Formulas used for CFD data processing and comparison with experimental data.	13
3.1	AMR function values for URANS $k-\epsilon$ simulation setup and subsequent solver instruction.	15
3.2	Comparison between URANS simulation setups characteristics. . . .	16
4.1	Definition of the AMR functions used for DES setups.	23
4.2	Time discretization used for DES setups.	25
A.1	Boundary conditions for the periodic simulation.	49
B.1	Fitting coefficient calculated after sine interpolation.	53

List of Figures

1.1	The core of an High Temperature Gas-cooled Reactor (HTGR) reproduced from [03].	2
1.2	MHTGR scaled model overview: a) cross section of the core, upper and lower plena and PIV experimental setup b) upper plenum dimensions c) core layout, C1 is the single opened channel d) a photo of the experiment facility and the velocity streamlines in the upper plenum from full-field measurements [Alw+19]	3
1.3	TR-PIV results obtained from a single jet mixing in the upper plenum for $Re_1=3413$ (left), $Re_3=7912$ (center), and $Re_5=12819$ (right). (a) Mean velocity vector fields and mean velocity magnitude contour (m/s), and color contours of (b) r.m.s fluctuating axial velocity v_{rms} (m/s). [Alw+19]	5
1.4	Normalized mean vertical velocity profiles obtained from TR-PIV measurements for various Reynolds and compared with results from studies of Milanovic and Hammad (2010)[MH10], and Fellouah et al. (2009)[FBP09]. [Alw+19].	6
2.1	Upper plenum plane section representation with dimensions in <i>mm</i> and the coordinate system used during TR-PIV tests.	8
2.2	3D computational domain geometry representation, the coordinate system adopted and the nomenclature used for each boundary.	9
2.3	Comparison between the experimental coordinate system and the CFD one.	10
2.4	A basic example of the Adaptive Mesh Refinement solver methodology.	11
2.5	One midpoint subdivision of a hexahedral cell: from a single cell, 8 child cells are generated.	12
2.6	Geometry representation of the line probes used for CFD velocity data collection.	13

3.1	Adaption cell size scalar scenes at $Z=0$ plane for three different mesh setups: a static uniform mesh 3.1a, a static refined mesh 3.1b and an AMR setup 3.1c. All simulations refer to the Re5 URANS case.	16
3.2	Comparison with the AMR function values 3.2a and the Adaption cell size scalar scenes 3.2b at $Z=0$ plane for the same URANS $k - \epsilon$ AMR setup	17
3.3	URANS $k - \epsilon$ static <i>uniform</i> mesh simulation: velocity magnitude scalar filed at $z = 0$ plane section with total pressure isolines and $y/D = 1,3,6,9$ line probes.	18
3.4	Comparison of velocity magnitude (top), vorticity magnitude and streamlines (center) and pressure coefficient (bottom) for the three Re5 URANS setups: <i>AMR</i> (left), <i>refined</i> (center) and <i>uniform</i> (right).	19
3.5	URANS $k - \epsilon$ mesh setups mean velocity results compared with 2D TR-PIV data.	20
4.1	Scalar scenes of Kolmogorov Length Scale (left figure 4.1a) and Taylor Microscale (right figure 4.1b) at the $Z=0$ plane section of the upper plenum, calculated from the uniform mesh RANS simulation.	22
4.2	Scalar scenes of the Adaption Cell size at $Z=0$ plane for the DES $\kappa - \epsilon$ static mesh setup.	23
4.3	Scalar scenes of the Adaption Cell size at $Z=0$ plane for the AMRv2.1 setup (up 4.3a) and for the AMRv2 setup (bottom 4.3b).	24
4.4	Local quantities \bar{v} and v'_{rms} monitored through time at a horizontal coordinate of 18 mm and a vertical coordinate of $y/D = 6$ (left), and $y/D = 9$ (right). The top plots show the local quantities \bar{v} and v'_{rms} calculated using a progressively increasing time period. The center plots show the ratio between the previous calculated quantities and the corresponding local experimental velocity. The bottom plots show the mean quantities time derivatives.	25
4.5	Cell count history for the DES setups.	26
4.6	Scalar scenes of the Delayed DES function field at $Z=0$ plane for the AMRv2.1 setup (up 4.6a) and for the static mesh setup (bottom 4.6b).	27
4.7	Scalar scenes of Convective Courant Number (CCN) for AMRv2.1 seutp (left figure 4.7a) and the static mesh setup (right figure 4.7b) at the $Z=0$ plane section of the upper plenum.	27
4.8	Scalar scenes of the Vorticity magnitude field at $Z=0$ plane for the AMRv2.1 setup (up 4.8a) and for the static mesh setup (bottom 4.8b).	28
4.9	Comparison between DES setups velocity mean vertical component at $Z=0$ plane and corresponding experimental data.	30
4.10	Comparison between DES setups velocity mean horizontal component at $Z=0$ plane and corresponding experimental data.	31

4.11	Comparison between DES setups root mean squared velocity fluctuation vertical component at $Z=0$ plane and corresponding experimental data.	32
4.12	Comparison between DES setups root mean squared velocity fluctuation horizontal component at $Z=0$ plane and corresponding experimental data.	33
4.13	Comparison between DES setups of the Reynolds stress $\overline{u'v'}$ at $Z=0$ plane and corresponding experimental data.	34
4.14	Comparison between DES setups velocity mean vertical component at $Y=0$ plane and corresponding experimental data.	35
4.15	Comparison between DES setups velocity mean horizontal component at $Y=0$ plane and corresponding experimental data.	36
4.16	Comparison between DES setups root mean squared velocity fluctuation vertical component at $Y=0$ plane and corresponding experimental data.	37
4.17	Comparison between DES setups root mean squared velocity fluctuation horizontal component at $Y=0$ plane and corresponding experimental data.	38
4.18	Comparison between DES setups of the Reynolds stress $\overline{u'v'}$ at $Y=0$ plane and corresponding experimental data.	39
5.1	Re5 setups comparison through the relative error representation at the $Z=0$ plane.	43
5.2	Re5 setups comparison through the relative error representation at the $Y=0$ plane.	44
5.3	Re5 setups comparison through the mean relative error representation at the $Z=0$ plane.	45
A.1	Inflow pipe geometry representation used for the periodic simulation.	49
A.2	Inflow pipe velocity scalar field at $Z=0$ plane in addition to the representation of the axial velocity profile at 4 different cross-section planes.	50
A.3	Scalar scenes of velocity components and turbulent kinetic energy at the periodic interface.	51
B.1	Space coordinates of the maximum vertical velocity through time at $y/D = 6$ and $y/D = 9$ planes, in addition with the sine interpolation plot. The position unit is meters, and time is expressed in seconds.	53

Chapter 1

Introduction

Engineering research about High Temperature Gas Cooled Reactor (HTGR) technology is highly focused onto the prediction of reactors' behaviour in normal and, more importantly, accidental scenarios, using modern computational tools.

Two main possible accident scenarios could be identified: one related to the coolant depressurization (DCC) and one to a power loss (PCC). Both ultimately affect the cooling system, specifically the physical nature of the heat exchange within the reactor [MC06].

The purpose of the problems launched by the American Society of Mechanical Engineers (ASME) V&V 30 Subcommittee on Verification and Validation in Computational Nuclear System Thermal Fluids Behavior is to develop more accurate CFD codes to support regulatory reviews [Eng21].

The next pages will report the development process of and the validation of multiple CFD simulations using a set of experimental data provided by the ASME. The aim of this thesis is to present multiple possible solutions to the benchmark problem number two: *"Benchmark Data for Validation of Computational Simulations of Nuclear System Thermal Fluids Behavior for the Texas A&M Upper Plenum Experimental Facility"*.

The main focus will be the comparison between TR-PIV and CFD results using also multiple Adaptive Mesh Refinement algorithms.

This first chapter will illustrate the details of the ASME benchmark problem no.2: its purpose, the instrumentation used for the experimental measurements, and the related data collected. Then, in chapter 2 the computational approach will be discussed. In chapters 3 and 4, the CFD solution obtained using two different physics models will be described and the numerical results will be compared with the experiments. Chapter 5 will provide a method to evaluate all the presented CFD setups by defining the relative error, and finally, chapter 6 will gather all the information from previous discussions for a proper conclusion and development of this work.

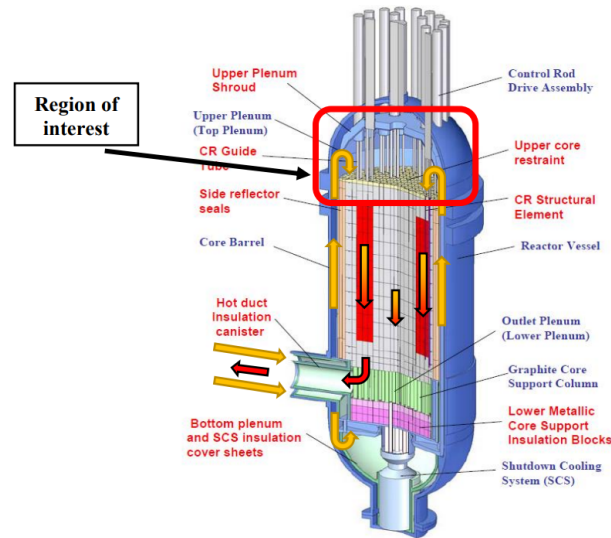


Figure 1.1: The core of an High Temperature Gas-cooled Reactor (HTGR) reproduced from [03].

The key points of the next chapters were also summarized in the presentation held at the 33rd Parallel Computational Fluid Dynamics International Conference (ParCFD 2022).

1.1 The ASME benchmark problem no. 2

The second V&V benchmark problem, *Single-Jet Computational Fluid Dynamics (CFD) Numeric Model Validation*, has been initiated for the 2019 V&V Symposium and involves simulating a single-jet and plume for single jet experiments at different Reynolds numbers.

An HTGR schematics is shown in figure 1.1. The red box highlights the upper plenum, which is the region of interest in this thesis. The ultimate goal of the problem no.2 is the study the flow characteristics of an isothermal jet mixing in the upper plenum volume and impinging on the top wall. Using the set of data provided by the ASME and organizers, one or multiple CFD simulations must be developed and validated.

1.2 Facility overview

The experimental facility is a 1 : 16th scaled down version of the Generation IV Modular High Temperature Gas Cooled Reactor (MHTGR) [McV+15]. The facility

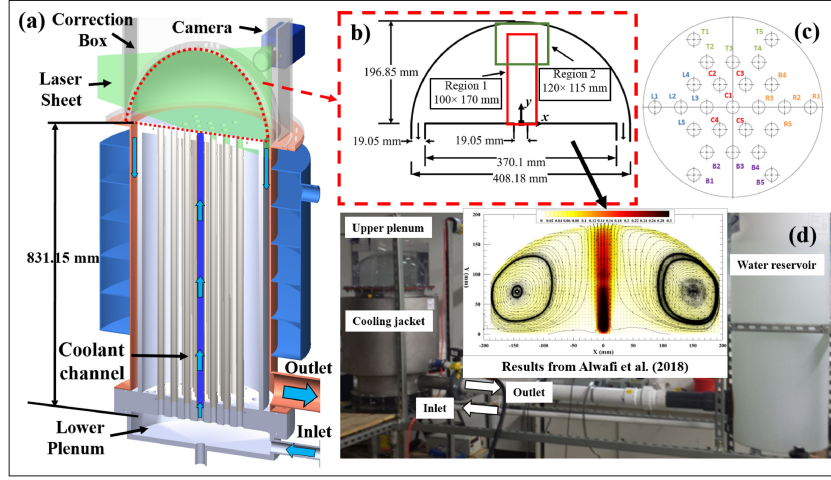


Figure 1.2: MHTGR scaled model overview: a) cross section of the core, upper and lower plena and PIV experimental setup b) upper plenum dimensions c) core layout, C1 is the single opened channel d) a photo of the experiment facility and the velocity streamlines in the upper plenum from full-field measurements [Alw+19]

is a closed loop and, as figure 1.2 shows, the primary components are the lower and upper plena, and the core connecting the two. The HTGR model is filled with water and the 2D time resolved Particle Image Velocimetry (2D TR-PIV) data are collected after steady state is achieved within the upper plenum. The entire flow field is resolved for five different Reynolds number calculated as follow:

$$Re = \frac{V_{avg} D_j}{\nu} \quad (1.1)$$

where V_{avg} is the mean bulk flow velocity at the inlet of the upper plenum, D_j is the coolant channel diameter, and ν is water kinematic viscosity at the plenum inlet temperature.

Water circulation within the reactor model is performed by a centrifugal pump. The mass flow rate is regulated using a variable frequency converter and measured by a flowmeter. In this way, the setup allows the execution of experimental tests at different Reynolds numbers, through the variation of the average velocity V_{avg} of the single jet flow coming from the inlet channel hole (indicated as C1 in figure 1.2).

The flowmeter data provides the inlet boundary conditions for the isothermal jet at the tested five different Reynolds numbers. The inlet results values are shown in table 1.1.

Set	Inlet mass flow rate [kg/s]	Re	Averaged inlet temperature [$^{\circ}C$]
1	0.05	3413	19.74
2	0.089	5963	19.74
3	0.118	7912	19.74
4	0.158	10622	19.74
5	0.19	12819	19.74

Table 1.1: Inlet conditions for different experimental sets.

1.3 Experiments and available data description

This section will be focused primarily on the results collected thanks to the experimental tests on the MHTGR model, with a brief description of the measurement techniques applied, by reference to the work of Alwafi et al. [Alw+19].

The 2D TR-PIV experimental setup, also showed in figure 1.2, consisted of a continuous laser and a high-speed camera with various frame rates, ranging from 400 Hz to 700 Hz. The seeding particles were polyethylene microsphere particles with an average diameter of $13 \mu m$ and a density of $1.002 g/cm^3$.

This setup was used for the resolution of the entire jet flow field at a section plane of the upper plenum, which corresponds to the $Z = 0$ plane in the adopted coordinate system. Some of the TR-PIV results are shown in figures 1.3 and 1.4.

The main results used for the validation process in this study are the mean velocity profiles and velocity fluctuation at 10 different y/D_j values, also referred to y/D for the sake of brevity.

In total, 50 data files, 10 for each Re number, are available for the study.

Each file consists of 7 columns reporting respectively: x coordinate (horizontal location in mm), y coordinate (vertical location in mm), \bar{u} (horizontal time-average velocity [m/s]), \bar{v} (vertical time-average velocity [m/s]), u'_{rms} (root-mean-square fluctuating horizontal time-average velocity [m/s]), v'_{rms} (root-mean-square fluctuating vertical time-average velocity [m/s]), $\overline{u'v'}$ (Reynolds stress [m^2/s^2]).

One example of collected data file is reported in table 1.2.

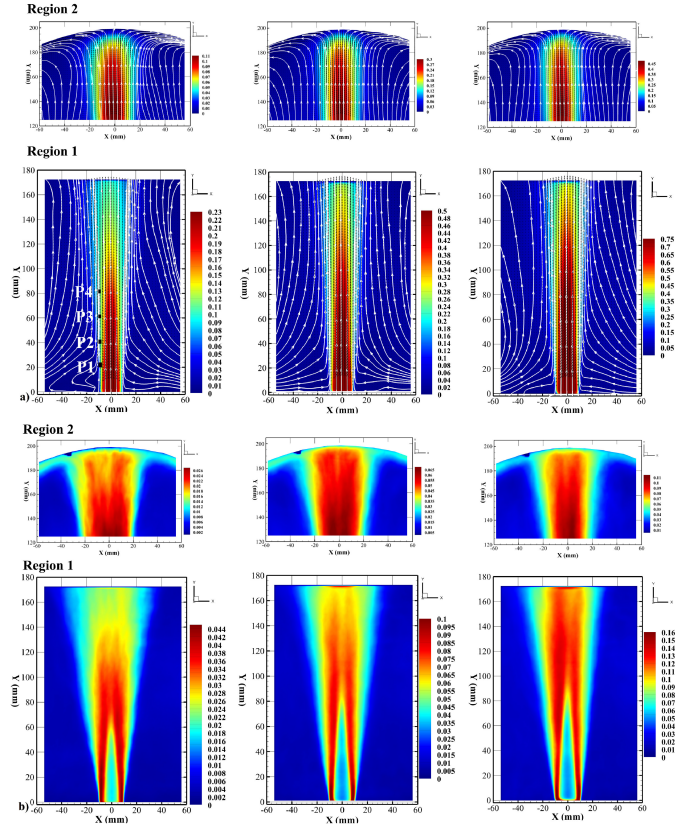


Figure 1.3: TR-PIV results obtained from a single jet mixing in the upper plenum for $Re_1=3413$ (left), $Re_3=7912$ (center), and $Re_5=12819$ (right). (a) Mean velocity vector fields and mean velocity magnitude contour (m/s), and color contours of (b) r.m.s fluctuating axial velocity v_{rms} (m/s). [Alw+19]

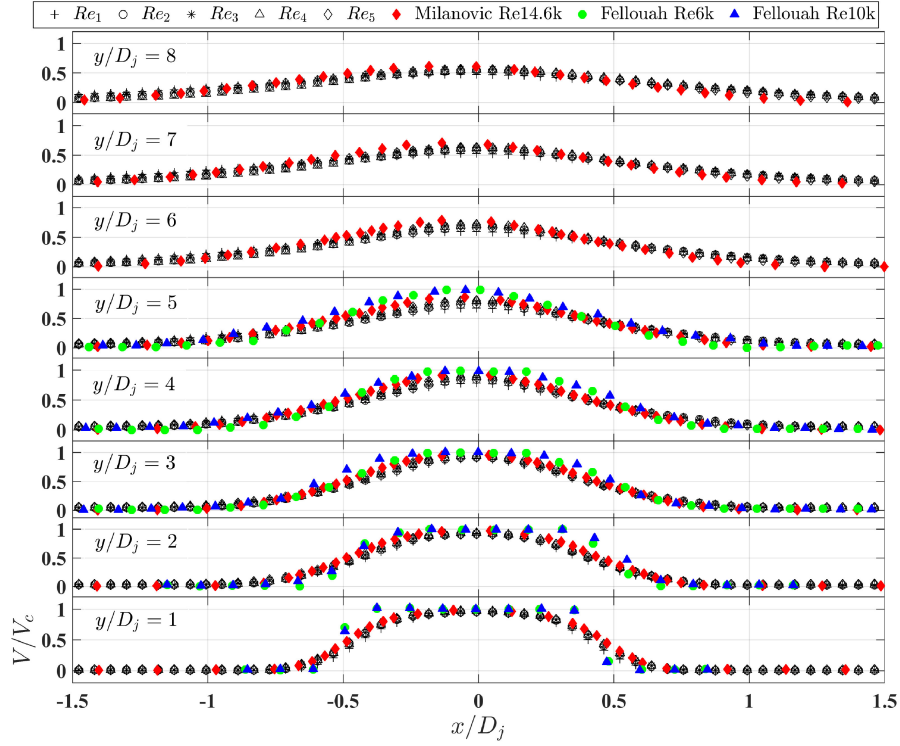


Figure 1.4: Normalized mean vertical velocity profiles obtained from TR-PIV measurements for various Reynolds and compared with results from studies of Milanovic and Hammad (2010)[MH10], and Fellouah et al. (2009)[FBP09]. [Alw+19].

x [mm]	y [mm]	\bar{u} [m/s]	\bar{v} [m/s]	u'_{rms} [m/s]	v'_{rms} [m/s]	$\overline{u'v'}$ [m ² /s ²]
-40.325253	171.450000	-0.004011	0.012730	0.011111	0.013218	0.000012
-39.921253	171.450000	-0.003766	0.013210	0.011229	0.013547	0.000009
-39.517253	171.450000	-0.003526	0.013745	0.011361	0.013926	0.000006
-39.113253	171.450000	-0.003303	0.014316	0.011527	0.014355	0.000004
-38.709253	171.450000	-0.003088	0.014918	0.011727	0.014847	0.000005
...
-0.733253	171.450000	-0.002479	0.389146	0.063309	0.093008	-0.000032
...
38.454747	171.450000	0.000678	0.016117	0.012863	0.016146	-0.000036
38.858747	171.450000	0.000888	0.015801	0.012607	0.0162186	-0.000034
39.262747	171.450000	0.001099	0.015541	0.012395	0.016341	-0.000034
39.666747	171.450000	0.001315	0.015319	0.012200	0.016495	-0.000035
40.070747	171.450000	0.001526	0.015048	0.011982	0.016590	-0.000036

Table 1.2: Example of experimental data table for Re5=12819 at $y/D = 9$.

Chapter 2

Simulations' outline

This chapter will summarise the general features of all the CFD setups described in the following chapters.

After a short description of the expected phenomenology, the first two sections will illustrate the upper plenum geometry transposition from the drawing to the simulation environment. Then, a brief section will focus on the boundary conditions and on some of the physical models used in the simulations.

The last two sections of this chapter will describe the Adaptive Mesh Refinement (AMR) model implemented in STAR-CCM+ and the algorithm used for every AMR simulation setup. Finally, the CFD data collection methodology will be described.

2.1 The impinging jet problem

The experimental data provided by the TR-PIV and described in chapter 1 led to a comparison based mainly upon velocity profiles. The upper plenum wall presence prevents a complete jet flow evolution along the axial coordinate, identified by the y axis in the representation of the experimental results in figure 1.3.

Figure 2.1 shows a dimensional¹ drawing of the upper plenum and anticipates the possibility of an impingement phenomenon at the top wall. Thus, the jet free flow theory applies just for a small number of diameters D along the axial coordinate. Moreover, the jet region dimensions will be highly affected by the plenum wall vicinity to the inlet surface. As an example, it will be impossible to evaluate the self-similar velocity profile due to the presence of the wall at y/D approximately around 10.

Despite the impingement, the typical axial velocity trends and the entrainment

¹Dimensions are provided by organizers.

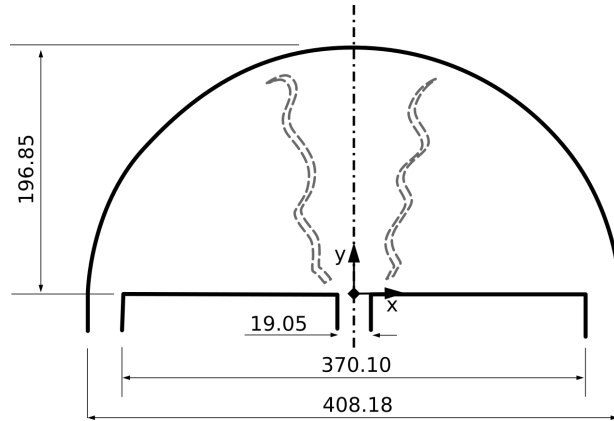


Figure 2.1: Upper plenum plane section representation with dimensions in *mm* and the coordinate system used during TR-PIV tests.

phenomenon can still be observed in the results in figure 1.4.

Figure 1.4 also introduces the effect of increasing Reynolds numbers: as the inlet velocity V_{avg} rises, a decrease in the jet flow x -wise dimension should have been noticed. However, since all Reynolds numbers have approximately the same order of magnitude (Re5 is only four times higher than Re1), the Reynolds influence is slightly detectable from the non-dimensional velocity profile comparison.

In conclusion, the free flow jet literature cannot be used for this specific jet flow field: the positive axial pressure gradient, induced by the upper plenum wall presence, alters the global flow layout.

This work will primarily illustrate the validation process of the algorithm that best suits the experimental velocity results, using the commercial CFD code Simcenter STAR-CCM+.

2.2 Computational domain

As mentioned in chapter 1, this work resumes the study by A. Froio, R. Zanino and A. Zappatore "*Validation of a non-isothermal-single-Jet CFD Model using STAR-CCM+*", where a 2D-axisymmetric geometry of the upper plenum was used for the simulation of the isothermal flow field.

A three-dimensional domain was required to represent non-axisymmetric effects and to overcome numerical instabilities as illustrated starting from chapter 3. The 3D plenum geometry was created by revolving the same 2D-axisymmetric domain around the axial direction. The result of the revolving operation is shown in figure 2.2. The main difference between the coordinate system used for CFD simulations and the one used for the TR-PIV tests is in the axis orientation and

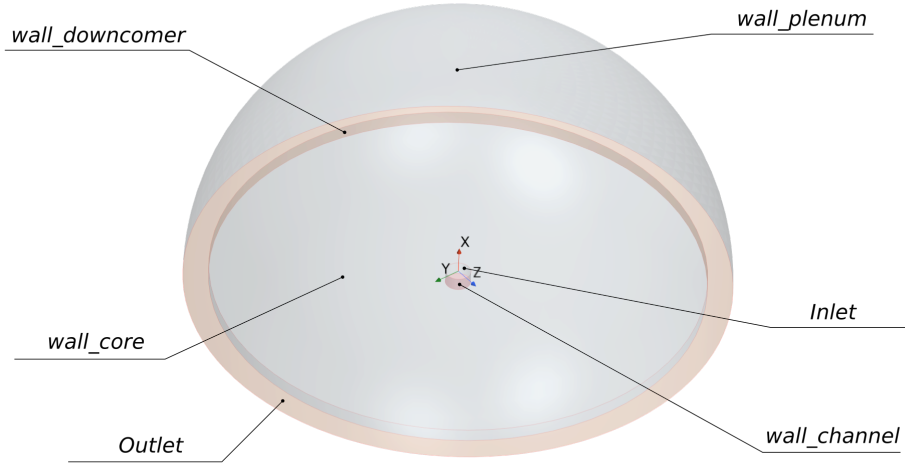


Figure 2.2: 3D computational domain geometry representation, the coordinate system adopted and the nomenclature used for each boundary.

in the velocity components denomination. In the computational domain, the vertical direction corresponds to the x -axis, while the TR-PIV results figure 1.3 addressed it as the y -axis. To keep continuity with the 2D-axisymmetric simulations, the coordinate system used for the 3D domain has not been changed. However, the experimental coordinate system orientation was adopted for the CFD results processing, visualization and validation.

Per contra, the CFD horizontal velocity component is v and corresponds to the experimental quantity u , while the vertical (or axial) CFD velocity component is u and corresponds to the experimental quantity v .

Figure 2.3 summarises the main differences between the CFD and the experimental coordinate systems.

Figure 2.2 highlights the boundary surfaces of the computational domain. Each boundary surface is then associated with the proper wall type in table 2.1.

The needed boundary values are the outlet pressure, which is set to a relative $0 Pa$, the velocity components and turbulent energy at the inlet.

Velocity inlet condition values, specifically velocity components and turbulent quantities, are set using tables obtained from periodic simulation results. For further details, please refer to appendix A.

As described in chapter 1, the working fluid within the HTGR model is water. The fluid properties have been calculated using the parameters in table 1.2 employing the IAPWS[PS07] database and are listed in table 2.2.

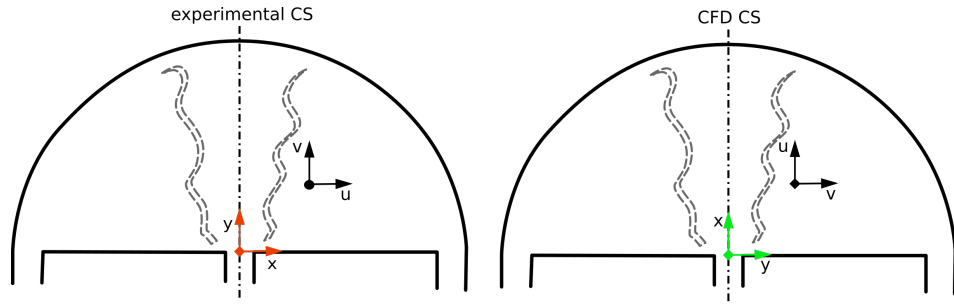


Figure 2.3: Comparison between the experimental coordinate system and the CFD one.

Inlet	Velocity Inlet
Outlet	Pressure Outlet
wall_channel	Wall no slip
wall_core	Wall no slip
wall_downcomer	Wall no slip
wall_plenum	Wall no slip

Table 2.1: Boundary conditions for the 3D computational domain.

Finally, since the isothermal state implies also a constant density, both RANS and DES models have been solved with a segregated flow method.

2.3 The Adaptive Mesh Refinement model

The Adaptive Mesh Refinement (AMR) model implemented in *Simcenter STAR-CCM+ 2021.2* [Sie21] actively changes the mesh size using a user-defined query criterion.

The solver can refine the selected elements or coarsen previously refined cells. This means that the AMR model cannot coarsen the user-generated mesh, which usually corresponds to the starting mesh.

The query criterion used in this work is the *User-Defined Mesh Adaption* criterion: this method utilizes a user-defined function to determine which cells should be refined, coarsened, or kept the same size.

The user-defined function, also called AMR function, usually takes into account both the spatial variations of the physical quantities that describe the inherent nature of the problem and an indicative dimension of each cell. A typical definition of the AMR function ϕ could state as follows:

$$\phi(\psi, \Delta) \equiv \nabla^2 \psi \cdot \Delta^2 \quad (2.1)$$

Dynamic Viscosity μ [$Pa \cdot s$]	$1.008 \cdot 10^{-3}$
Density ρ [kg/m^3]	998.26

Table 2.2: Water physical properties used for CFD simulations.

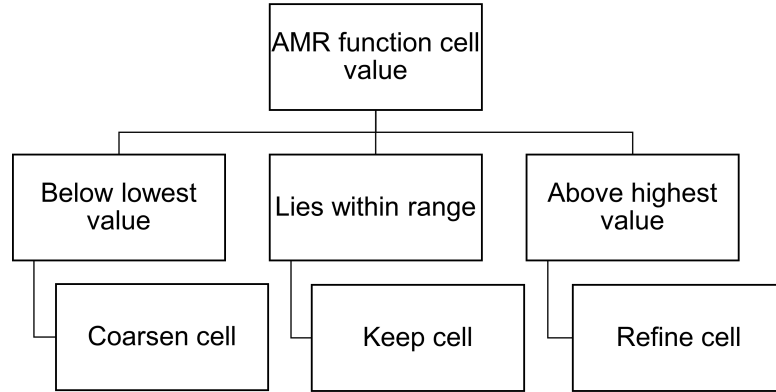


Figure 2.4: A basic example of the Adaptive Mesh Refinement solver methodology.

where $\psi = \psi(x, y, z, t)$ is the scalar field of the selected physical quantity, and $\Delta = \Delta(x, y, z, t)$ is the *adaption cell size* which is doubled the highest distance between the cell centroid and a vertex. As a result, the AMR function is also a scalar field that depends on both space and time: $\phi = \phi(x, y, z, t)$.

However, since negative gradients should also be taken into account, the previous definition has been modified with the laplacian modulus:

$$\phi(\psi, \Delta) \equiv |\nabla^2 \psi| \cdot \Delta^2 \quad (2.2)$$

The user then chooses two AMR function values that define a range. Then, the solver behaviour should be specified by choosing between three simple commands: "refine" "keep" and "coarsen". One possible outcome of this simple algorithm is shown in figure 2.4. If the cell AMR function value is below the lower limit, the solver refines that cell. If the cell value lies above the upper limit, then the solver coarsens the cell (only if previously refined). The cell is kept the same size if the value lies within the range.

The AMR function is usually directly proportional to a spatial variation of a physical quantity as shown in definition 2.2. This type of definition allows the user to restrain the spatial variations in order to generate a smoother transition of the physical solution: this could eventually increase the physical accuracy in

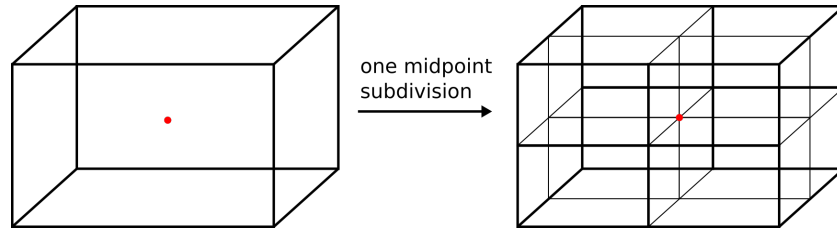


Figure 2.5: One midpoint subdivision of a hexahedral cell: from a single cell, 8 child cells are generated.

certain portions of the domain and decrease the cells needed elsewhere. In addition, definition 2.2 allows the refinement of those cells with high laplacian modulus values since both high positive and low negative values indicate strong physical variations.

This is the algorithm implemented in this study, and the corresponding solver behaviour is the one previously shown in figure 2.4.

The adaptive refinement process consists of one or multiple midpoint subdivisions. Each midpoint subdivision could generate from 8 to 15 child cells from one cell. An example in figure 2.5 shows one step of midpoint subdivision for a hexahedral cell.

The AMR model properties allow to set a maximum number of midpoint subdivisions and a minimum cell size: the refinement process goes on until one of these two constraints is met. If the adaption cell size of a child cell is lower than the minimum cell size limit, then that cell does not undergo refinement.

After a new refinement, the solver interpolates the solution onto the new mesh and each cell is queried again.

The mesh refinement frequency can be set on the basis of a number of iterations, usually for steady simulations, or on the basis of the number of time steps for unsteady simulations.

2.4 CFD data collection

With the entire three-dimensional flow field available for the validation process, it was necessary to prescribe the most effective way to compare the CFD results with the experimental data.

Since the TR-PIV results were collected at a 2D section of the upper plenum, it was decided to reproduce the same conditions within the computational domain through the monitoring of selected physical quantities on a plane section.

The two velocity components within the plane were exported using multiple line probes at different y/D coordinates ($y/D = 1,3,6,9$) in compliance with the experiments. Every line probe lies in the section plane selected as shown in figure

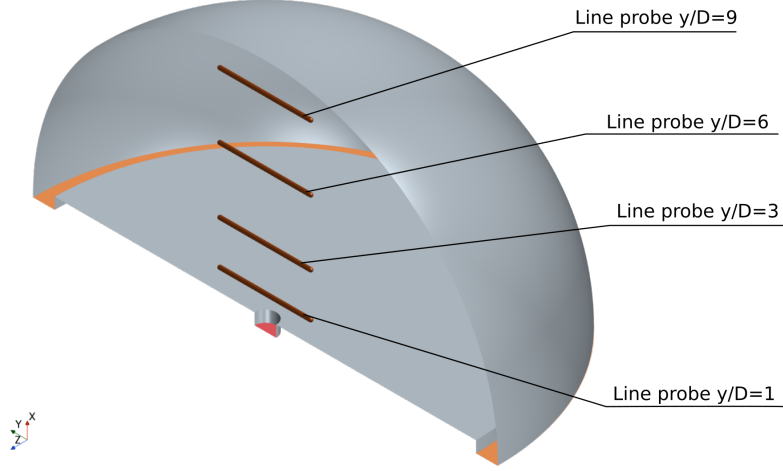


Figure 2.6: Geometry representation of the line probes used for CFD velocity data collection.

2.6.

For unsteady simulations, it was also necessary to set the exportation frequency of the velocity components at the selected line probes. A constant frequency of 50 Hz was chosen to facilitate the post-processing calculations.

The post-processing code reads each exported file and then determines the average velocities \bar{u} and \bar{v} , the root mean squared velocity fluctuations u'_{rms} and v'_{rms} , and the mean Reynolds stress $\overline{u'v'}$, for each line probe. The results consist of a total of 5 profiles varying along the x coordinate for each y/D .

The code implements the definitions listed in table 2.3 and then compares the results with the experimental data and other CFD setups.

$\bar{u}(x) = \frac{1}{T} \int_0^T u(x, t) dt$	$\bar{v}(x) = \frac{1}{T} \int_0^T v(x, t) dt$
$u'_{rms}(x) = \frac{1}{T} \sqrt{\int_0^T (u(x, t) - \bar{u}(x))^2 dt}$	$v'_{rms}(x) = \frac{1}{T} \sqrt{\int_0^T (v(x, t) - \bar{v}(x))^2 dt}$
$\overline{u'v'}(x) = \frac{1}{T} \int_0^T (u(x, t) - \bar{u}(x))(v(x, t) - \bar{v}(x)) dt$	

Table 2.3: Formulas used for CFD data processing and comparison with experimental data.

Note that fluctuation velocities and the Reynolds stress have been calculated only for DES setups, while for RANS simulations only mean velocities could be determined.

Chapter 3

Re5 URANS $\kappa - \epsilon$ case study

The highest Reynolds number conditions are considered to be the most challenging and computationally demanding due to the strong velocity and pressure gradients presence.

Thus, the focus of this Master's thesis is the validation of the Re5 simulations as they could be easily adjusted for lower Reynolds numbers.

However, the rising of numerical instabilities due to the high Reynolds number (Re5=12819) forced a shift to a 2nd order implicit time scheme. The overall physical time was chosen according to a preliminary jet oscillation study explained in appendix B.

After a brief description of the mesh discretization used for unsteady RANS (URANS) simulations, this chapter will discuss the CFD results compared with the experimental results.

The effectiveness of the AMR model implemented in two RANS setups will be also evaluated in the last section of this chapter.

3.1 Mesh setups definition

Three different setups have been simulated to highlight the AMR algorithm potential: two with a static mesh, and one with an active mesh.

The two static setups differ in the mesh configuration. The one identified as *uniform* is composed of a 2 mm size mesh grid for the whole domain (with the exception of the prism layer cells), while the one identified as *refined* has 2 mm size cells in the jet flow area on a background of 10 mm size mesh.

The AMR function selected for the AMR setup is called *Total Pressure Laplacian AMR*, and it is defined as follows:

$$\phi_{TP} \equiv |\nabla^2 P_{tot_{rel}}| \cdot \Delta^2 \quad (3.1)$$

The previous definition could be further expanded for a better comprehension of the main dependent variables:

$$\begin{aligned}\phi_{TP}(p_{rel}, V, \Delta) &\equiv \left| \nabla \cdot \nabla \left(p + \frac{1}{2} \rho |V|^2 - p_{ref} \right) \right| \cdot \Delta^2 = \\ &= \left| \left[\nabla^2(p - p_{ref}) + \frac{1}{2} \rho \nabla^2 |V|^2 \right] \right| \Delta^2 = \left| \left[\nabla^2 p_{rel} + \frac{1}{2} \rho \nabla^2 |V|^2 \right] \right| \Delta^2\end{aligned}\quad (3.2)$$

The main variables that concur to the function value in each cell are the relative pressure p_{rel} , simply called *pressure* in STAR-CCM+, the cell velocity V and the *adaption cell size* Δ . So, ϕ_{TP} is a scalar field measured in Pascals that changes in time and space.

After various attempts, the selected ϕ_{TP} "keep" range is: [1 20] Pa. Above the ϕ_{TP} value of 20 Pa, the solver refines the selected cells; if the ϕ_{TP} cell value is below 1 Pa, then the solver coarsens the cell only if it was refined in the previous AMR trigger. This strategy is summarized in the table 3.1.

$\phi_{TP} > 20 Pa$	\rightarrow	refine cell
$1 Pa < \phi_{TP} < 20 Pa$	\rightarrow	keep cell
$\phi_{TP} < 1 Pa$	\rightarrow	coarsen cell

Table 3.1: AMR function values for URANS k- ϵ simulation setup and subsequent solver instruction.

This configuration will be denominated as *AMR* for this RANS subcase.

The starting discretization for the AMR setup was a 40 mm uniform mesh, with a minimum possible cell size of 2 mm. The maximum midpoint subdivisions allowed are three and the AMR solver is triggered every time step.

The three meshes are displayed in figure 3.1. The *static* meshes are independent of time, while the *adaptive* mesh representation refers to a particular time instant: $t = 45 s$.

As a result, the AMR setup shows a concentration of cells within the jet flow area showing a more optimized calculation coupled with a computational cost reduction. Table 3.2 shows how the AMR setup uses the lowest number of cells.

Table 3.2 also shows that the Convective Courant Number is closer to 1 in the AMR simulation than in the other setups. So, the AMR space discretization could be considered the most effective amongst the presented setup.

The local ϕ_{TP} values and the corresponding adaption cell size are shown in figure 3.2. From the adaption cell size representation it is possible to see that the cells within jet flow area have been refined and most of the AMR function values lie within the green area equivalent to "keep" range. A few of cells in the jet core have

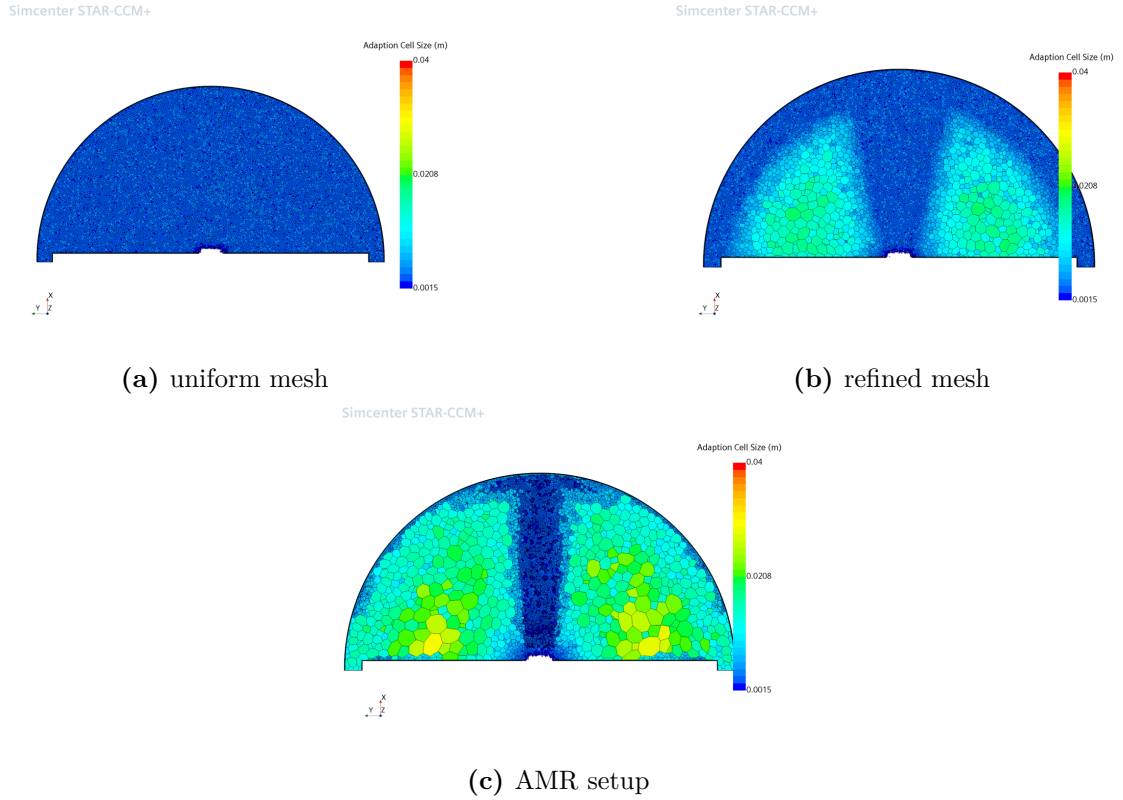
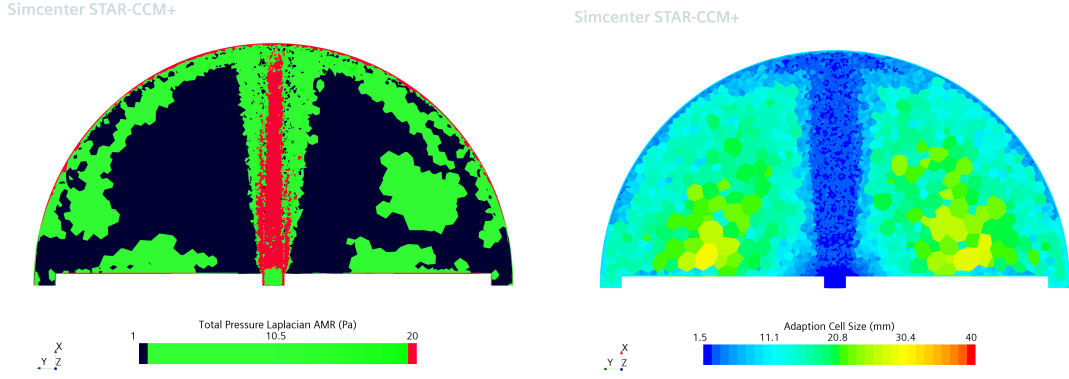


Figure 3.1: Adaption cell size scalar scenes at $Z=0$ plane for three different mesh setups: a static uniform mesh 3.1a, a static refined mesh 3.1b and an AMR setup 3.1c. All simulations refer to the Re5 URANS case.

	Static uniform	Static refined	AMR
Time step duration [s]	0.1	0.1	0.1
Maximum inner iterations	100	100	100
Time simulated [s]	31.0	19.9	45.0
Mean CCN	3.67	2.52	1.76
Mean number of cells	$3.25 \cdot 10^6$	$1.9 \cdot 10^6$	$0.48 \cdot 10^6$

Table 3.2: Comparison between URANS simulation setups characteristics.

an AMR function value above 20 Pa, however, they have not been refined further as one of the two limitations has been reached. Figure 3.2b proves the existence of a large number of approximately 2 mm size cells. So, the encountered constrain could be the minimum cell size. Cells in the dark blue, from figure 3.2a, are not coarsened as they belong to the starting mesh generated before the AMR solver intervention.



(a) AMR function scalar field at Z=0 plane (b) Adaption cell size scalar field at Z=0 plane

Figure 3.2: Comparison with the AMR function values 3.2a and the Adaption cell size scalar scenes 3.2b at Z=0 plane for the same URANS $k - \epsilon$ AMR setup

3.2 Results

After enough time has been simulated, it is possible to examine the total pressure and velocity fields through the representation in figure 3.3.

Both velocity scene and total pressure contours suggest that the potential core, where total pressure is constant, ends between $y/D = 1$ and $y/D = 3$. For $1 < y/D < 3$, the velocity and the total pressure start to decrease: the viscous dissipation and the entrainment phenomenon contribute to the jet flow deceleration and enlargement. Since the RANS simulations could solve only the mean flow field, it is impossible to locate where the jet breakdown into multiple vortexes occurs.

Figure 3.4 compares the three setups using three main physical quantities: velocity magnitude, vorticity magnitude, and pressure coefficient¹.

The pressure coefficient representation provides more information about the jet flow field behaviour: as the velocity and the total pressure decrease, the static pressure drops from 0.01 to approximately 0, for $y/D > 1$. At $y/D = 6$ the static pressure starts to rise as the flow approaches the upper wall: since the problem is highly subsonic, the wall presence is perceived upstream and the flow streamlines start to bend accordingly. The static pressure coefficient continues to rise for higher

¹The used pressure coefficient is: $c_p = \frac{p_{rel}}{\frac{1}{2}\rho V_{avg}^2}$, where p_{rel} is the relative pressure, and ρ and V_{avg} are respectively the water density and the average velocity at the inlet surface.

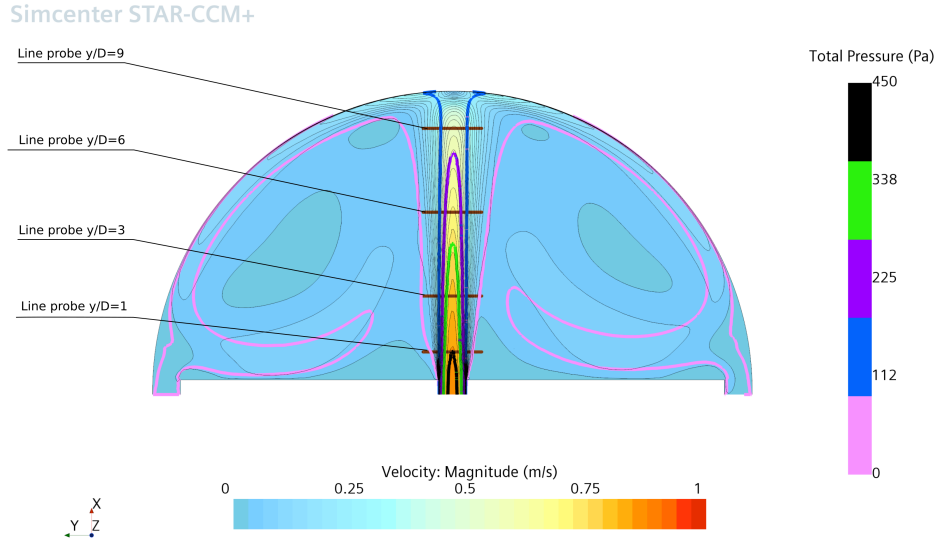


Figure 3.3: URANS $k - \epsilon$ static *uniform* mesh simulation: velocity magnitude scalar filed at $z = 0$ plane section with total pressure isolines and $y/D = 1, 3, 6, 9$ line probes.

y/D reaching a maximum of 0.3^2 at the upper wall: this means that before the stagnation point the velocity has been intensely reduced by the viscous effect. The result of the impingement is the formation of a toroidal vortex outside the jet flow area.

Overall, the CFD velocity field resembles the experimental one in figure 1.3.

The validation process resumes with the analysis of the results gathered using the line probes. Figure 3.5 shows the comparison between the two static mesh setups, the AMR setups and the TR-PIV data about the mean velocity.

Both figure 3.4 and figure 3.5 show a good match between the results from all three URANS setups and the experiments. So, it is possible to state that the URANS $\kappa - \epsilon$ AMR setup is able to reach the required physical precision with the least number of cells, thus reducing the overall computational cost.

However, the average horizontal component profile $\bar{v}(x)$ at $y/D = 9$ is different from the experimental one despite the chosen CFD setups: the possible reasons will be discussed in the final chapter of this work.

On the basis of these results, it is possible to conclude that three types of URANS setup have been validated using mean velocity data from TR-PIV. From both experiment and CFD results, it is possible to affirm that the use of a 3D domain is

²The value $c_p = 0.3$ is out of scale, otherwise figure 3.4 would have been hard to read.

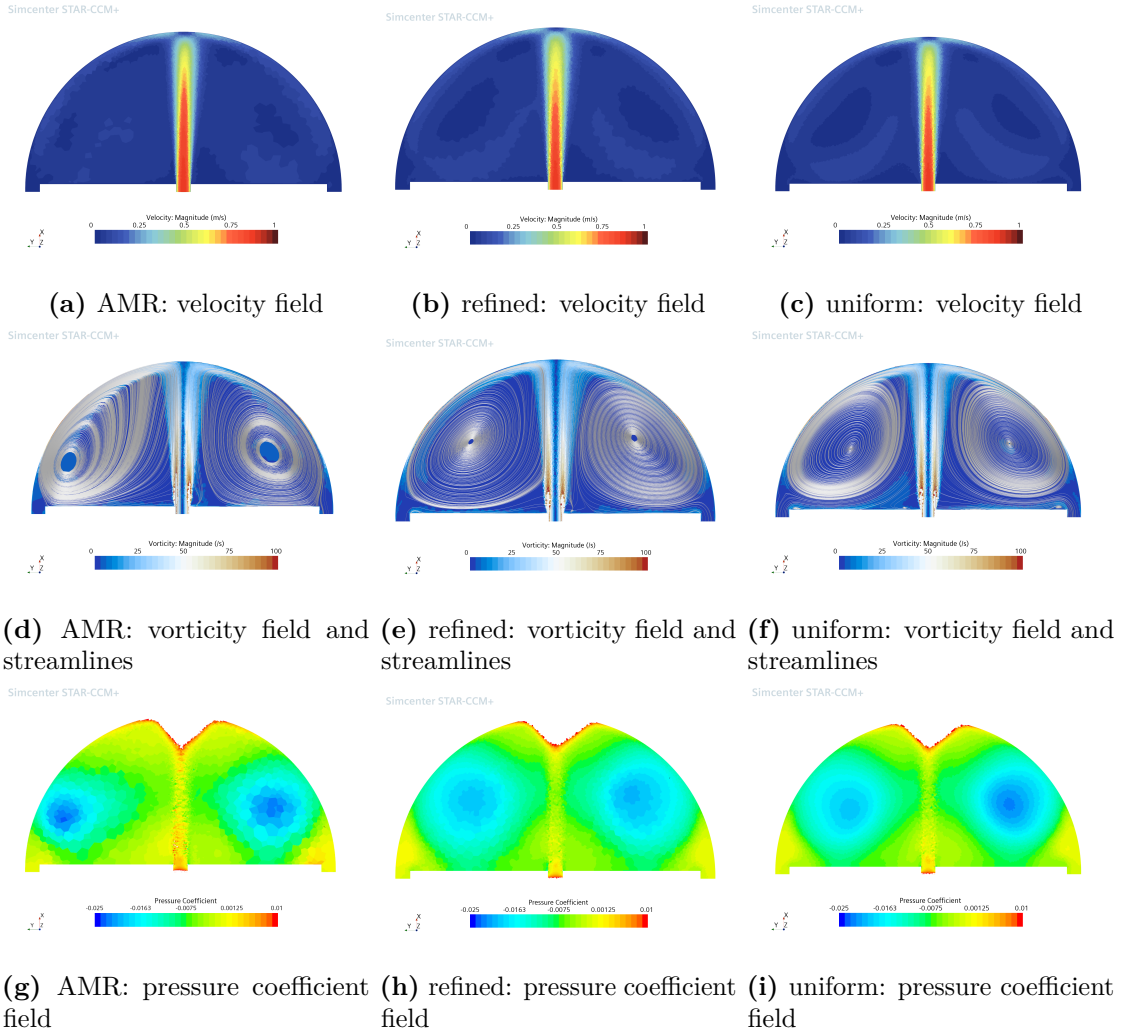


Figure 3.4: Comparison of velocity magnitude (top), vorticity magnitude and streamlines (center) and pressure coefficient (bottom) for the three Re5 URANS setups: *AMR* (left), *refined* (center) and *uniform* (right).

motivated by the asymmetry of all the represented velocity profiles. These simulations, however, cannot provide any results about the velocity fluctuations since the RANS equations usage. In order to obtain a complete validation, using also the remaining TR-PIV data, it was necessary to change the used RANS model into DES: the results will be discussed in the next chapter. The analysis carried out in this chapter could be considered the first step towards a more complete answer to the benchmark problem. The three URANS simulations represent the lightest and fastest way to obtain a reliable mean velocity field.

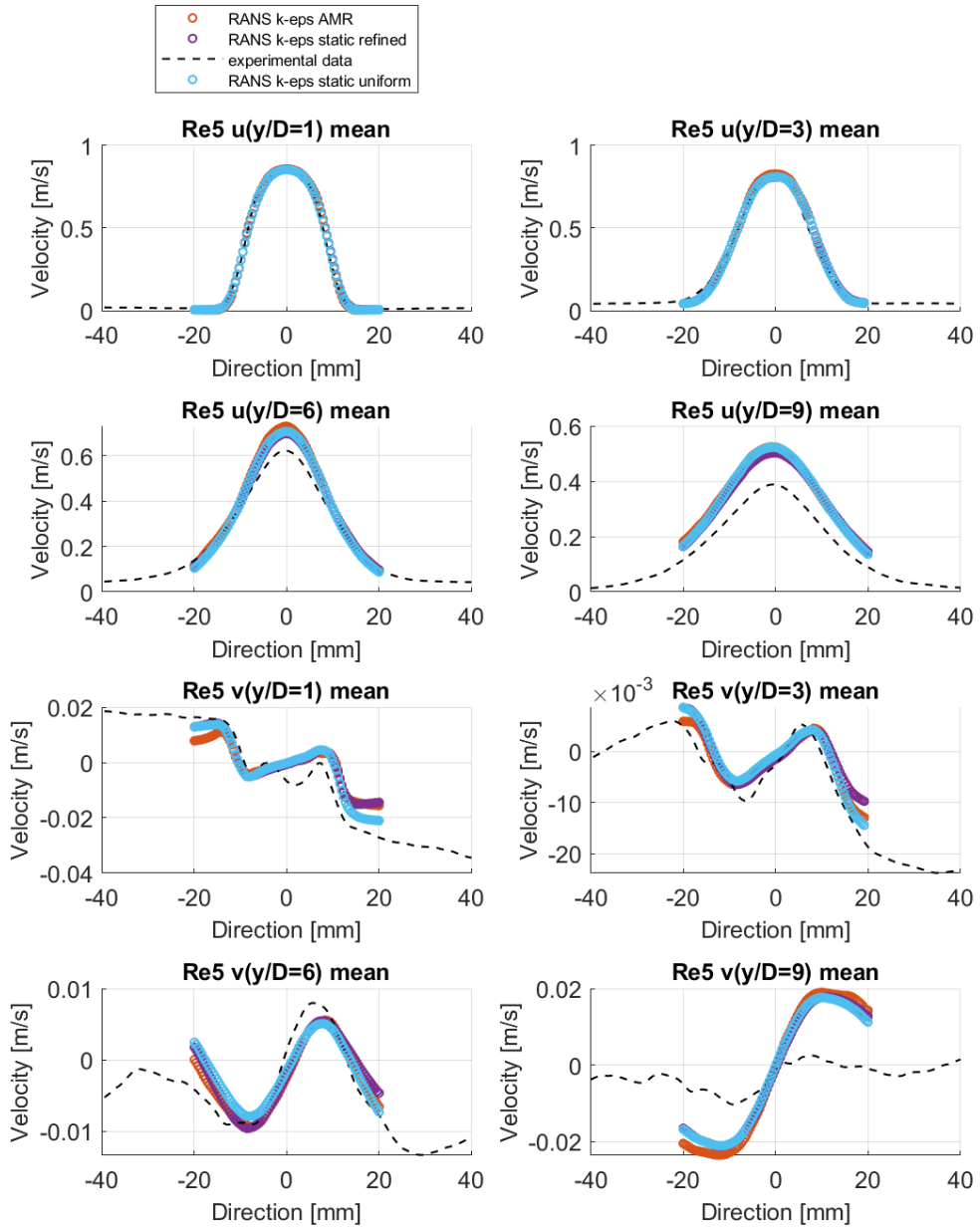


Figure 3.5: URANS $k - \epsilon$ mesh setups mean velocity results compared with 2D TR-PIV data.

Chapter 4

Re5 DES case study

The further step towards a more accurate solution, without exceeding a reasonable limit of needed computational resources, is the Detached Eddy Simulation (DES) model implementation.

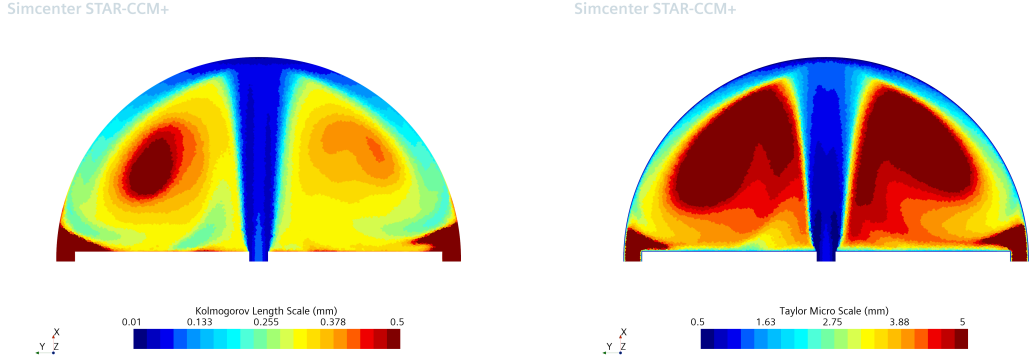
The DES model is a hybrid model which incorporates the use both the Large Eddy Simulation (LES) model (far from the wall) and the RANS model (near the wall). Some changes are required in both static and AMR setup. Following the STAR-CCM+ guide, the requirements that should be met involve the cell size in the key areas of the domain, and the Courant number distribution within the upper plenum. Also, the inlet boundary requires the introduction of the Synthetic Eddy Method (SEM) [Jar+06] through new conditions. Thanks to the SEM, the turbulent flow field is seen as a superposition of spinning eddies whose size is determined by the turbulence scales. The use of the SEM conditions at the domain inlet boundary approximates the presence of turbulence and produces a limited number of small eddies, which are then transported by the jet mean flow.

The first simulated setups use the Delayed Detached Eddy Simulation (DDES) Elliptic Blending (EB) $\kappa - \epsilon$: in this way it was possible to analyze the effect of the DES model with respect to the previous RANS results, keeping the same turbulence model.

The Improved Delayed Detached Eddy Simulation (IDDES) SST Menter $\kappa - \omega$ model is also used for one static mesh setup: the reason was to evaluate possible effects on the solution near the upper wall, specifically at $y/D = 9$.

4.1 Mesh changes for DES

To capture most of the turbulence spectrum, also enabling the use of LES, the cell size value Δ should lie between the Taylor microscale λ and the Kolmogorov length scale η : $\lambda > \Delta > \eta$.



(a) Kolmogorov length scale scalar field at $Z=0$ (b) Taylor Micro scale scalar field at $Z=0$

Figure 4.1: Scalar scenes of Kolmogorov Length Scale (left figure 4.1a) and Taylor Microscale (right figure 4.1b) at the $Z=0$ plane section of the upper plenum, calculated from the uniform mesh RANS simulation.

Both scales can be evaluated from previous RANS simulations, thus estimating one of the possible discretizations. The values of both scales are displayed in figure 4.1.

As a result, it is possible to distinguish two main regions in the domain:

- a conical area within the jet flow, in the middle of the domain, where $\lambda \approx 0.5 \text{ mm}$ and $\eta \approx 0.02 \text{ mm}$
- the external region of the jet flow, where $\lambda \approx 10 \text{ mm}$ and $\eta \approx 1 \text{ mm}$

Considering the scales values, the static mesh used as a reference has a 0.5 mm conical volumetric control at the center of the domain. The mesh outside the cone has a 2 mm base size. This specific choice was made taking into account the available computational resources and the elapsed real time required for an unsteady DES. The resulting static mesh shown in figure 4.2 has a total of $7.63 \cdot 10^6$ elements. Some trials with halved volumetric control base size showed that about 10^8 cells are generated. This type of mesh was considered too costly at this stage of the study.

The static mesh definition also set a background mesh for the AMR setups: a 2 mm uniform mesh. The minimum cell size limit within the AMR setups was set to 0.5 mm.

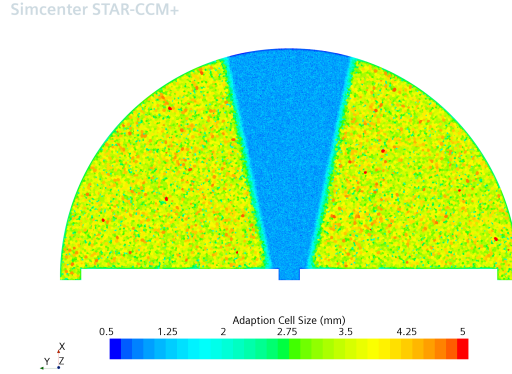


Figure 4.2: Scalar scenes of the Adaption Cell size at $Z=0$ plane for the DES $\kappa - \epsilon$ static mesh setup.

4.2 DES AMR setups definition

Definition 2.2 of the AMR function has been slightly modified to locate the refinement process within the jet flow area. The new definition states:

$$\begin{cases} \phi = |\nabla^2 \psi| \cdot \Delta^2 & r \leq 50 \text{ mm} \\ \phi = 0 & r > 50 \text{ mm} \end{cases} \quad (4.1)$$

This new definition suggests that the actual area subjected to the AMR solver is delimited by a cylinder parallel to the x axis and with a radius of $r = 50 \text{ mm}$ ¹.

For the DES case, multiple physical quantities were chosen as function ψ : the objective was to investigate the possible effect of the choice of ψ upon the grid and on the final solution. Table 4.1 summarises all the selected variables and the relative setup name.

Physical quantity	Keep range	Setup name
Pressure	$[2 \ 20] \text{ Pa}$	AMRpL
Velocity magnitude	$[0.1 \ 0.25] \text{ m/s}$	AMRvL
Total Pressure	$[-1 \ 100] \text{ Pa}$	AMRv2
	$[20 \ 100] \text{ Pa}$	AMRv2.1

Table 4.1: Definition of the AMR functions used for DES setups.

AMRv2 and AMRv2.1 setups differ in the lower limit value of "keep" range: recalling definitions 4.1 and 2.2, 0 is the lowest value of ϕ , and since the AMR solver can only

¹The coordinate r refers to a cylindrical coordinate system and it is defined as: $r = \sqrt{y^2 + z^2}$.

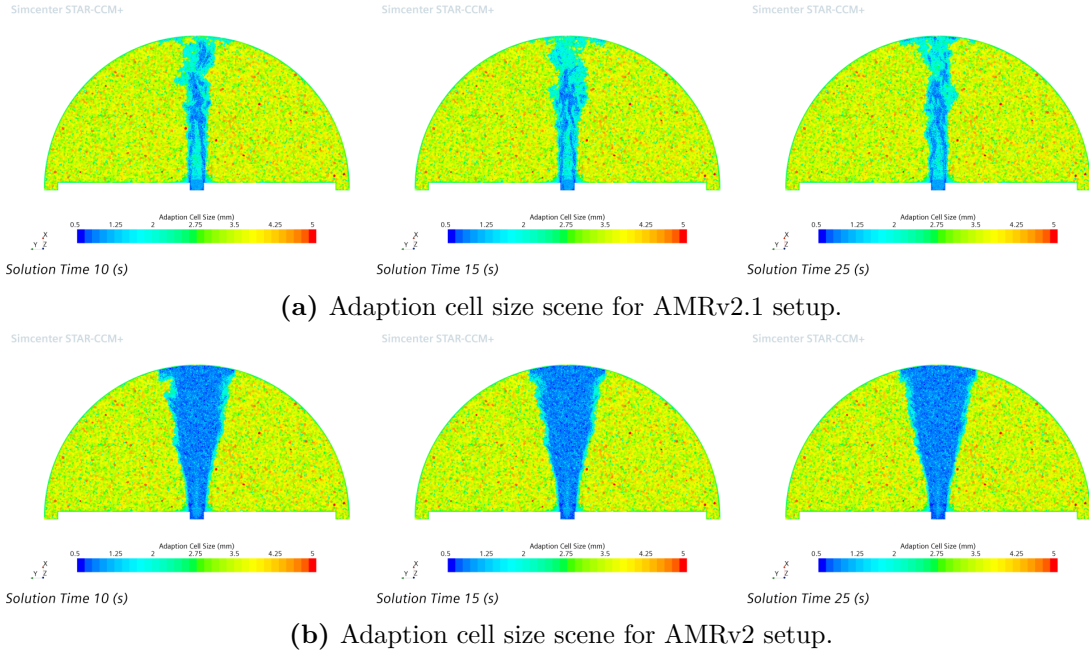


Figure 4.3: Scalar scenes of the Adaption Cell size at $Z=0$ plane for the AMRv2.1 setup (up 4.3a) and for the AMRv2 setup (bottom 4.3b).

coarsen previously refined cells, AMRv2 mesh will be refined exclusively. While, for the remaining AMR setups, the mesh within the 50 mm radius cylinder can be refined or coarsened as the solution changes through time. This behaviour is highlighted by figure 4.3 where the adaption cell size is represented.

Figure 4.3 shows how the AMRv2.1 setup actively changes the mesh size according to the physical solution changes through time. The AMRv2 setup always refines the cells involved in physical phenomena: the result is a conical shape similar to the volumetric control used for RANS *refine* setup and DES static simulations.

The time discretization was set in order to have a Convective Courant number not far from 1 within the jet flow area, without excessively extending the required elapsed real-time.

The best compromise was reached by setting residual-based stopping criteria summarised in table 4.2.

The total physical time selection for DES setups was verified using a 60 seconds static simulation: the aim was to achieve a relatively small time variation of the mean velocities using the least possible amount of computational resources. The local quantities \bar{v} and v'_{rms} were monitored through time at a horizontal coordinate of 18 mm and a vertical coordinate of $y/D = 6$, and $y/D = 9$. As will be

Time-step duration [s]	0.001
Minimum number of inner iterations	9
Maximum number of inner iterations	30
Inner iteration criterion	all residuals < 0.002

Table 4.2: Time discretization used for DES setups.

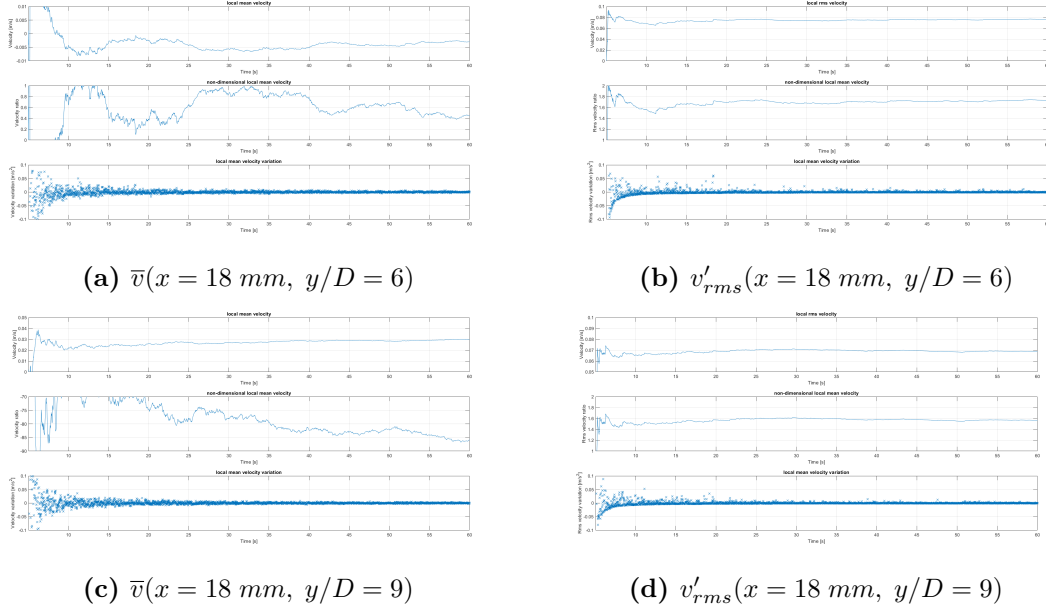


Figure 4.4: Local quantities \bar{v} and v'_{rms} monitored through time at a horizontal coordinate of 18 mm and a vertical coordinate of $y/D = 6$ (left), and $y/D = 9$ (right). The top plots show the local quantities \bar{v} and v'_{rms} calculated using a progressively increasing time period. The center plots show the ratio between the previous calculated quantities and the corresponding local experimental velocity. The bottom plots show the mean quantities time derivatives.

demonstrated in the next sections, the horizontal component is highly subjected to significant variation velocity through time, especially near the impingement zone. Figure 4.4 reports in the top plots the local quantities \bar{v} and v'_{rms} calculated using a progressively increasing time period. In addition, the ratio between the previous quantities and the corresponding local experimental velocity is also represented in the plots at the center of the figure. Finally, the bottom plots show the mean quantities time derivatives.

From the top and bottom plots, it is possible to conclude that 25 seconds of simulation time is enough to reach a satisfactory steady-state. So, a total of 25

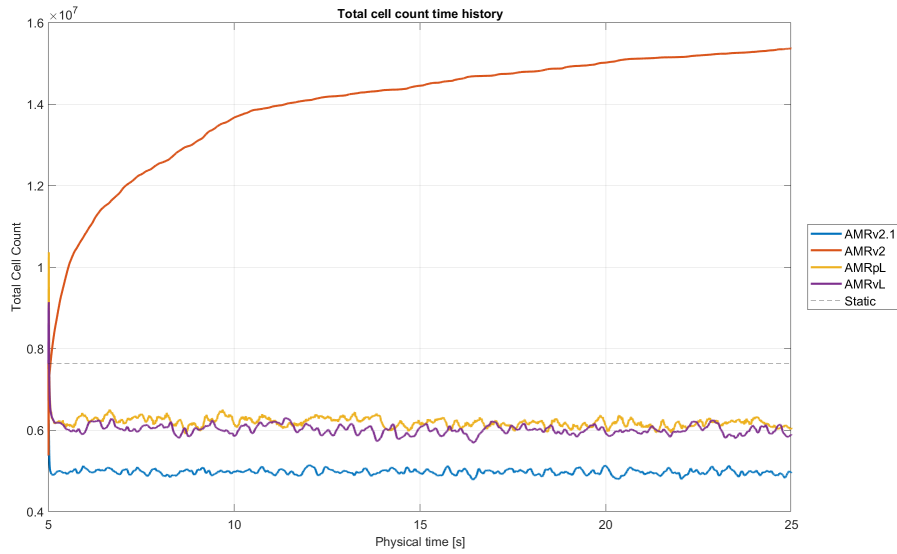


Figure 4.5: Cell count history for the DES setups.

seconds have been simulated for every DES setup. Then, the first 5 seconds were not considered for the result processing.

As the solution advances in time, so does the active refinement: starting from the background mesh, the number of cells needed to meet the AMR algorithm requirements can change in time. So, it is possible to evaluate the AMR behaviour through the total cell count monitor for each simulation. Figure 4.5 shows the total cell count throughout time: as predicted the AMRv2 has the highest number of cells, while all the other AMR setups showed a considerable reduction in the total element count. The AMRv2.1 setup presents the highest cell reduction, using approximately $2 \cdot 10^6$ cells less than the static mesh setup.

4.3 Results

The adopted DES model created a decomposition of the domain in three different regions, characterized by different sets of equations: the LES zone, the near-wall RANS zone, and the blending zone. The aim was to force through the mesh discretization the use of LES solver within the jet flow area and the use of RANS for the boundary layer. Scene 4.6 proves that this objective has been reached throughout the entire simulated time in both static mesh and AMR setups. Both figures 4.6a and 4.6b report the Delayed DES function at the $Z=0$ plane; according to the STAR-CCM+ guide, this function indicates which type of approach is used by the solver within the domain: if this function is equal to 1 then the LES model is used; if the function value is 0, then RANS model is used; values between 0 and

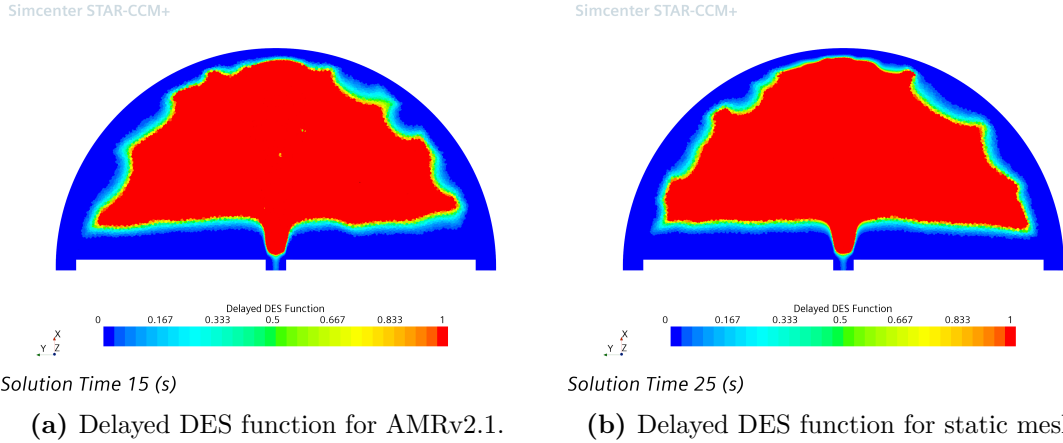


Figure 4.6: Scalar scenes of the Delayed DES function field at $Z=0$ plane for the AMRv2.1 setup (up 4.6a) and for the static mesh setup (bottom 4.6b).

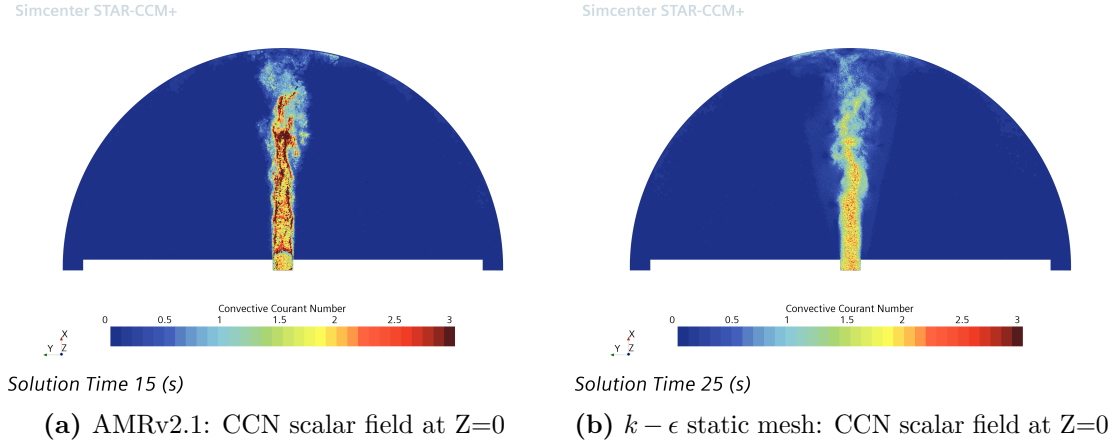


Figure 4.7: Scalar scenes of Convective Courant Number (CCN) for AMRv2.1 setup (left figure 4.7a) and the static mesh setup (right figure 4.7b) at the $Z=0$ plane section of the upper plenum.

1 indicate that the blending model is used.

The other parameter that was monitored is the Convective Courant number (CCN) reported in figure 4.7.

One consequence of the AMR solver use is the CCN increase in some cells within the jet flow field: all AMR setups showed that a higher number of cells reaches a peak of $CCN = 3$. Despite this effect, all the AMR setups were considered valid. This CCN increase could be explained by looking at the adaption cell size scalar field: the AMR solver tends to generate cells smaller than the 0.5 mm limit; since

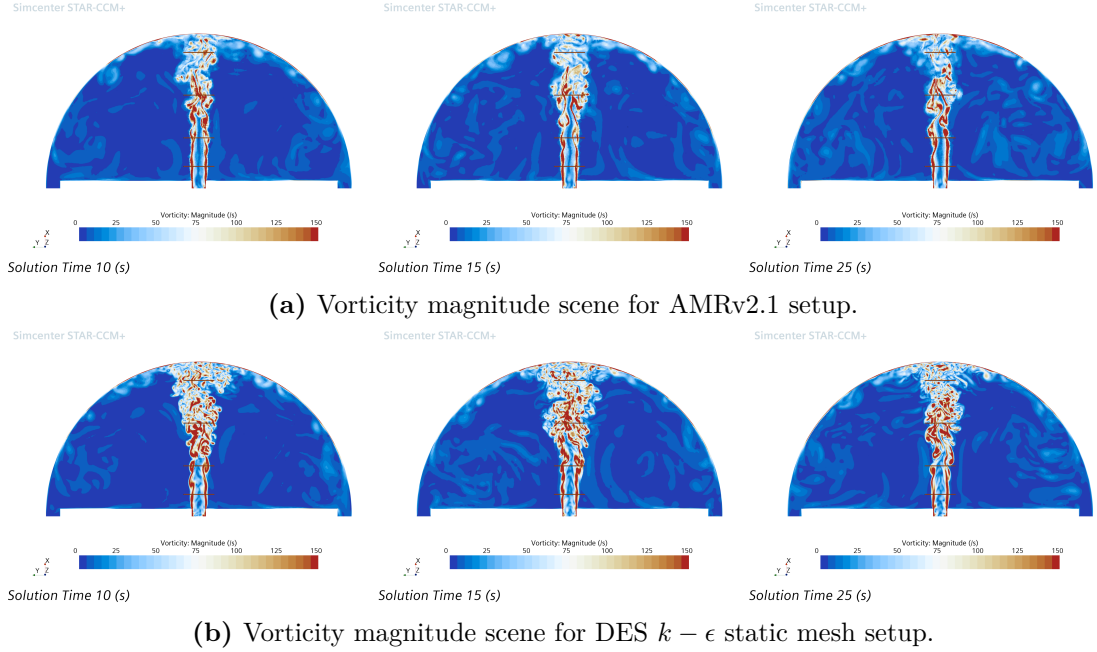


Figure 4.8: Scalar scenes of the Vorticity magnitude field at $Z=0$ plane for the AMRv2.1 setup (up 4.8a) and for the static mesh setup (bottom 4.8b).

the time step is fixed and considering the local velocity constant, then a smaller cell means a higher CCN. This issue could be overcome by reducing the time step, however, the simulation elapsed real time needed to reach 25 seconds of simulation time will increase.

From the vorticity representation in figure 4.8, it is possible to recognize the main turbulent structures within the domain throughout time.

More information can be deduced from 4.8: the potential core zone ends between $y/D = 1$ and $y/D = 3$ as previously discovered from RANS simulations; then, between $y/D = 3$ and $y/D = 6$, the jet starts to break into multiple vortexes; these structures reach the upper plenum wall and then start to descend following the dome wall where they are dissipated by the boundary layer action, thanks to the no-slip condition. Thus, the mean flow field is consistent with the one previously analyzed through RANS simulations.

The comparison of the AMRv2.1 vorticity scene throughout time shows that part of the jet flow field structures is being cut off due to the AMR solver behaviour. However, both this chapter and the next one will demonstrate that all the AMR setup results can be considered still consistent with the experimental data and the results of the static mesh setup.

To evaluate the accordance with experiments, velocity components along $y/D = 1, 3, 6, 9$ line probes were exported at a constant delta time of 0.020 s . This particular choice was made in order to limit the maximum number of .csv files generated by one simulation², hence avoiding possible buffer issues and required post-processing memory overloading. So, a sampling frequency of 50 Hz was set to ease the data handling and visualization.

Two sets of line probes were used for the results calculations, one set lies in the $Z=0$ plane, and the other lies in the $Y=0$ plane: the purpose of the use of two perpendicular planes was to comprehend how this could affect the solution and the relative error from the experimental data since the exact TR-PIV plane cannot be located in the domain.

After at least 20 seconds, enough data were available for each simulation processing. Following the formula reported in table 2.3, the results at $Z=0$ plane were plotted in figures 4.9, 4.10, 4.11, 4.12, and 4.13 at the end of this chapter. The same set of results has been calculated at the $Y=0$ plane and reported in figures 4.14, 4.15, 4.16, 4.17, and 4.18, located also at the end of the current chapter.

Through the analysis of all the previous figures, a good match between the CFD results and the experimental data for the mean vertical component \bar{u} is observed at every y/D coordinate.

However, the results concerning the mean horizontal component \bar{v} show that: as y/D increases, all the CFD setups solution tends to move away from the expected results, especially at $y/D = 9$. Here, the experimental horizontal component is lower than predicted and even the implementation of the IDDES model could not clarify the cause.

A different trend is observed for the fluctuation results: as y/D increases, the match with experiments improves. This, ultimately affects the stresses $\overline{u'v'}$ overall match, which improves at higher y/D .

Both sets of results, at $Z=0$ plane and $Y=0$ plane, show the same behaviour, so it is possible to conclude that the solution is lightly affected by the selected plane, probably because a consistent steady-state has been reached.

²For each simulation 8 line probes are monitored (4 probes at $Z=0$ plane and 4 probes at $Y=0$ plane); each line probe export 2 velocity component (horizontal and vertical) every 0.02 seconds. Therefore, for a 25 seconds simulation a total of: $8 \cdot 2 \cdot 25/0.02 = 20000$.csv files are generated.

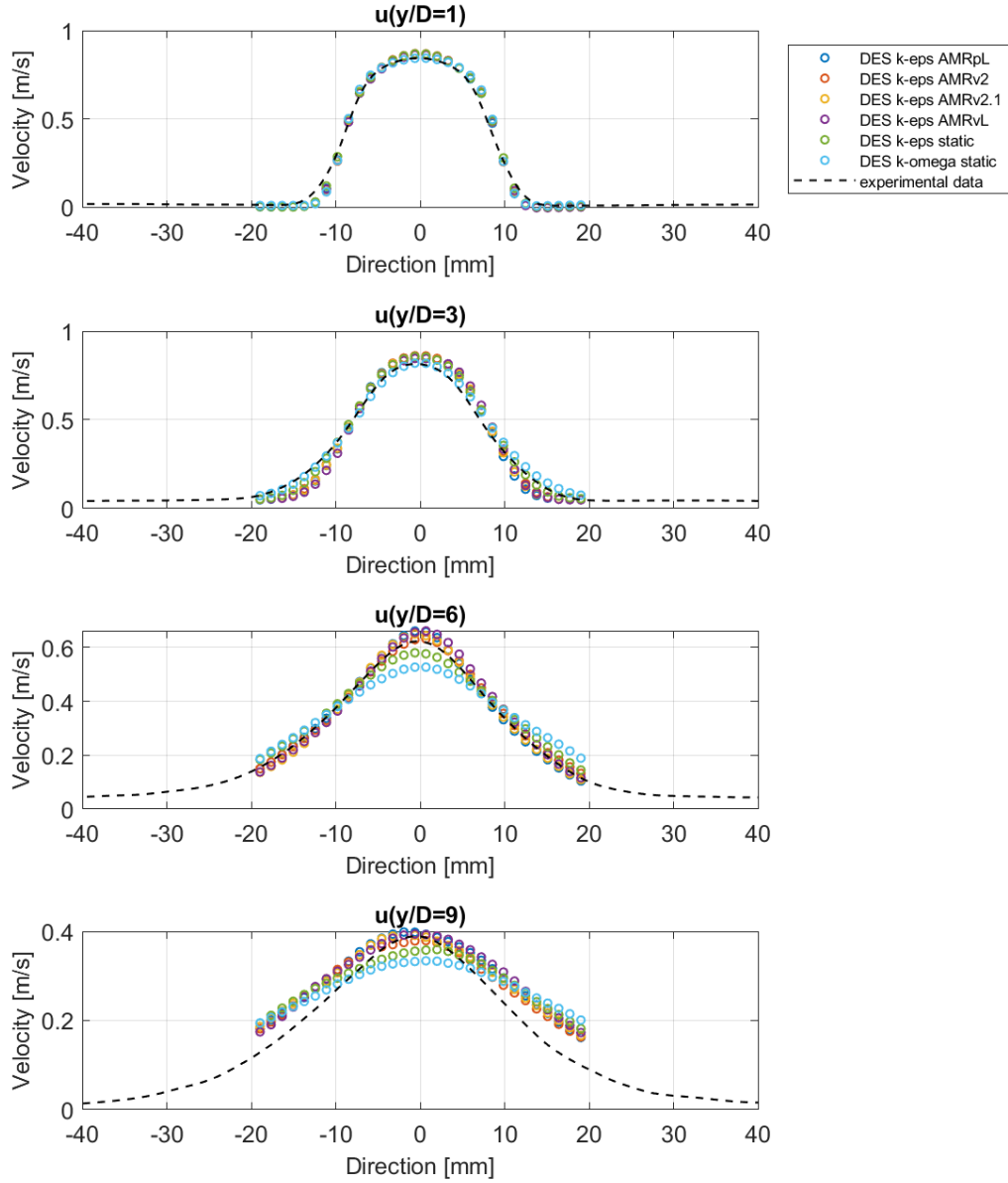


Figure 4.9: Comparison between DES setups velocity mean vertical component at $Z=0$ plane and corresponding experimental data.

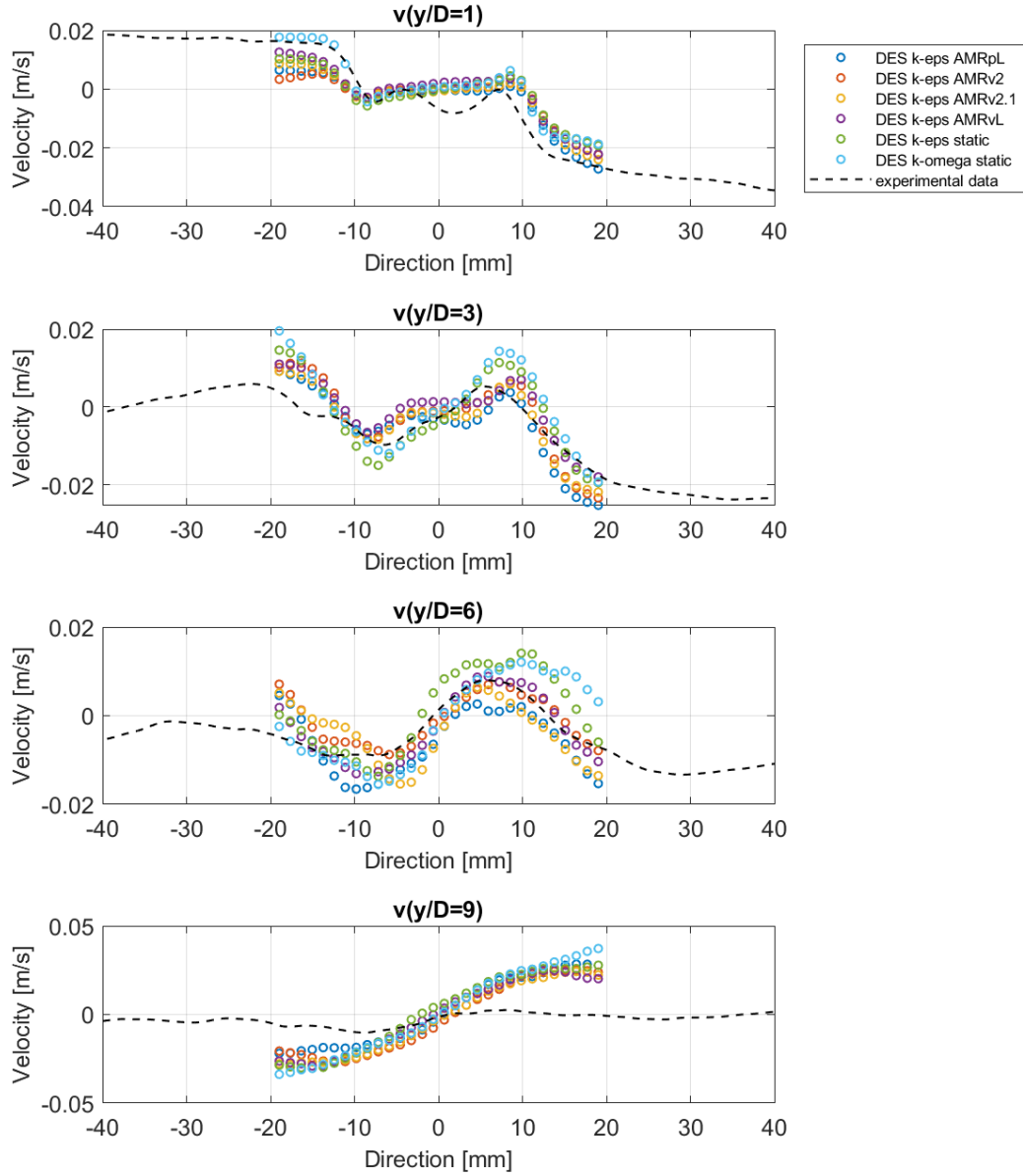


Figure 4.10: Comparison between DES setups velocity mean horizontal component at $Z=0$ plane and corresponding experimental data.

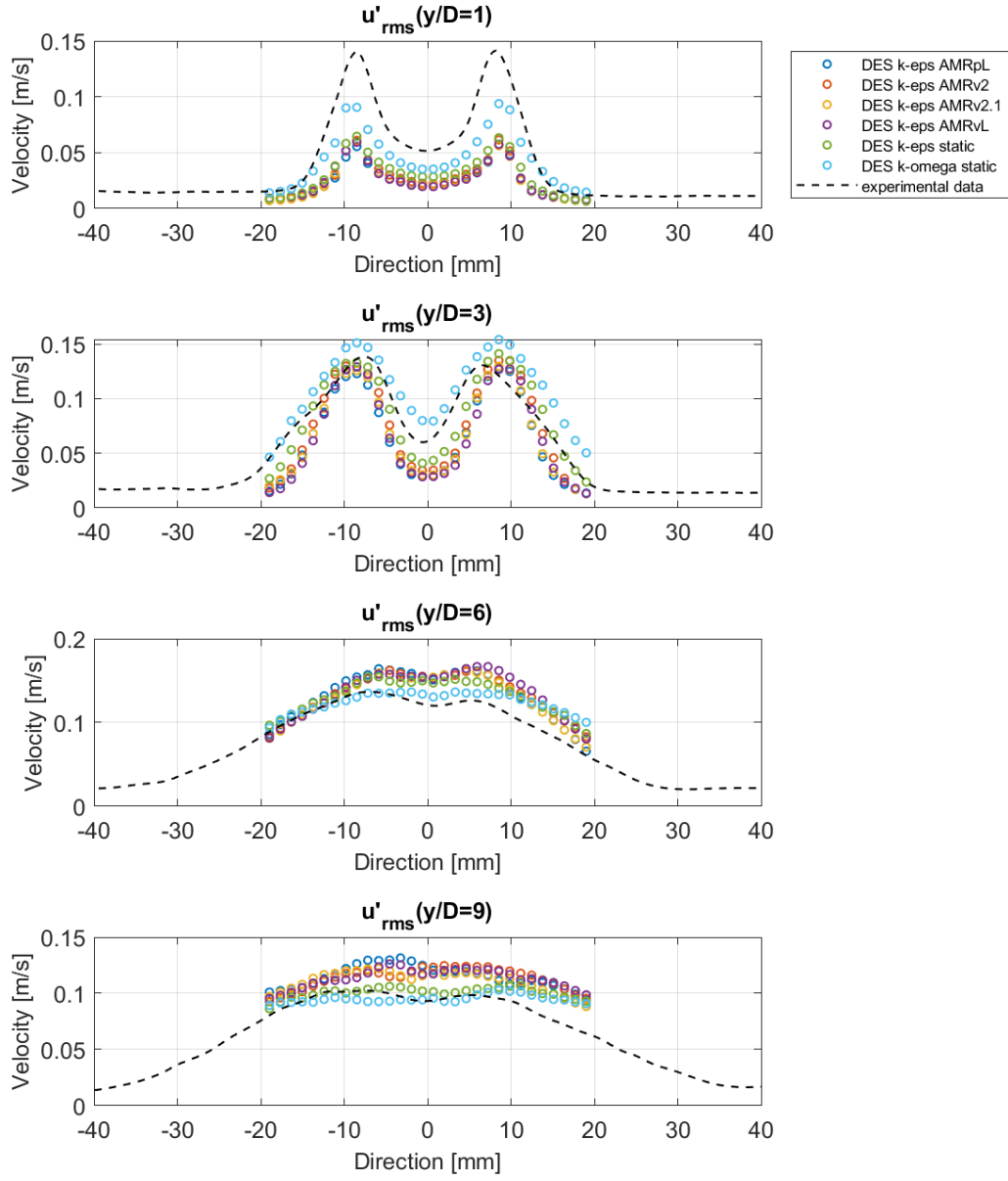


Figure 4.11: Comparison between DES setups root mean squared velocity fluctuation vertical component at $Z=0$ plane and corresponding experimental data.

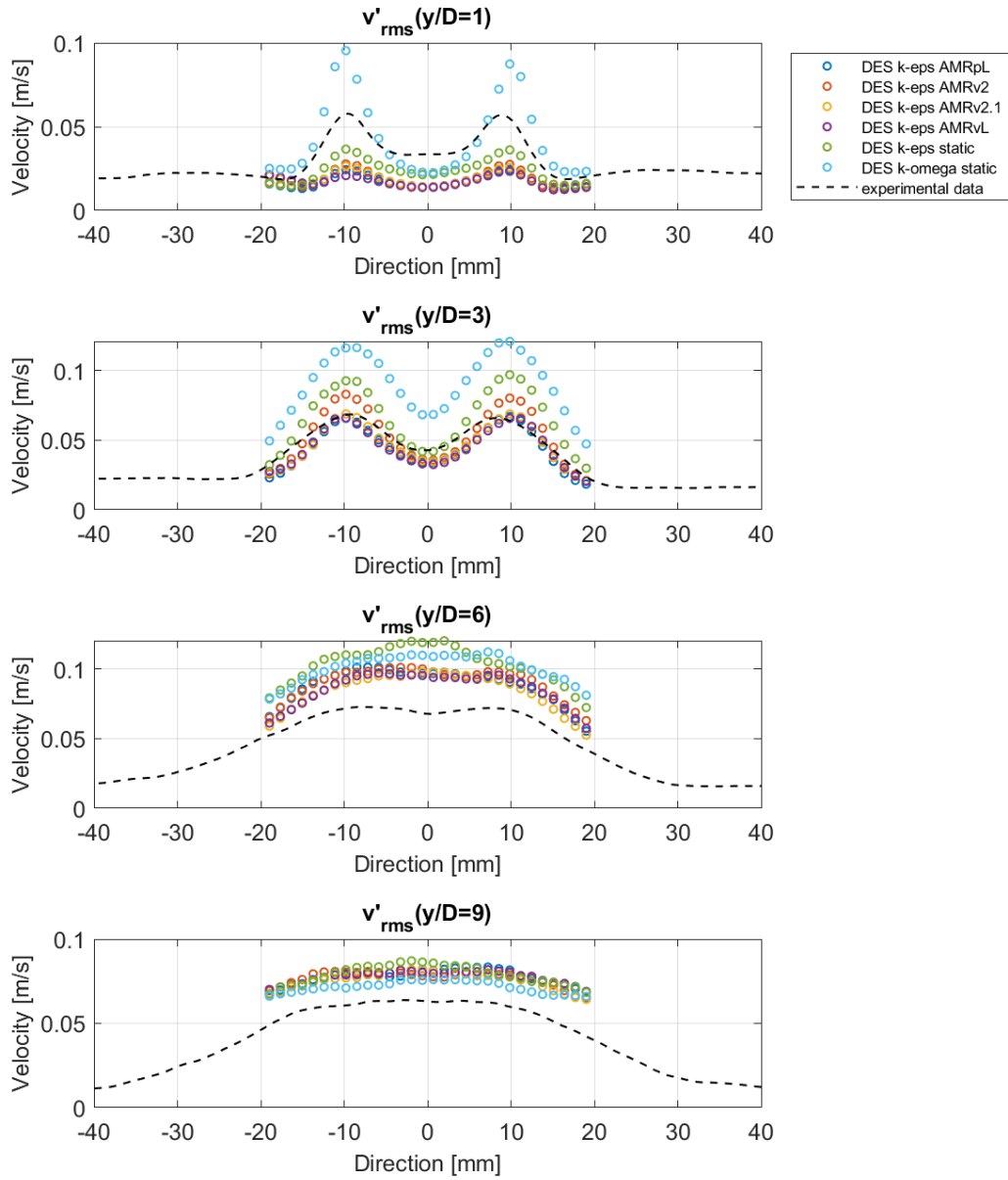


Figure 4.12: Comparison between DES setups root mean squared velocity fluctuation horizontal component at $Z=0$ plane and corresponding experimental data.

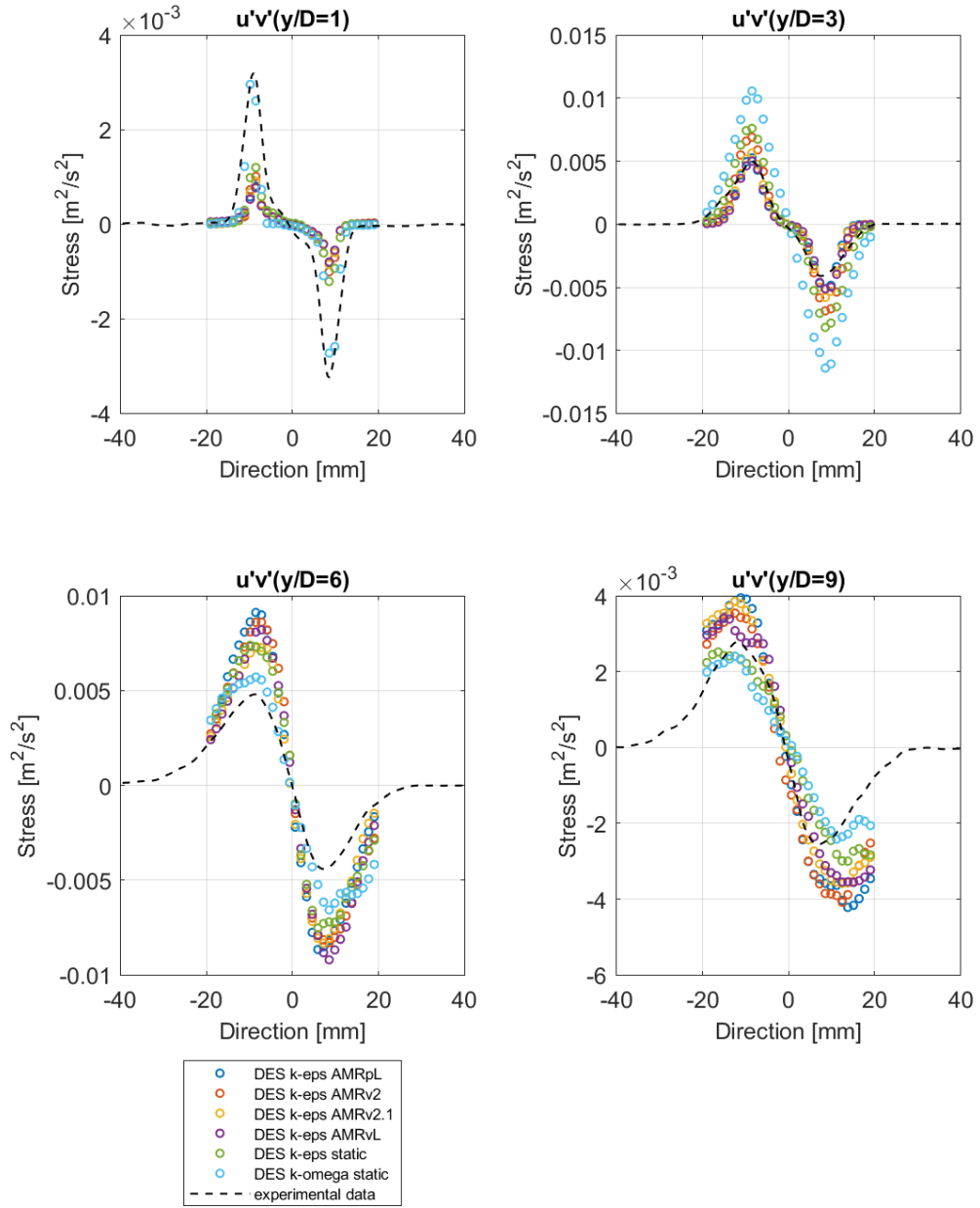


Figure 4.13: Comparison between DES setups of the Reynolds stress $\overline{u'v'}$ at $Z=0$ plane and corresponding experimental data.

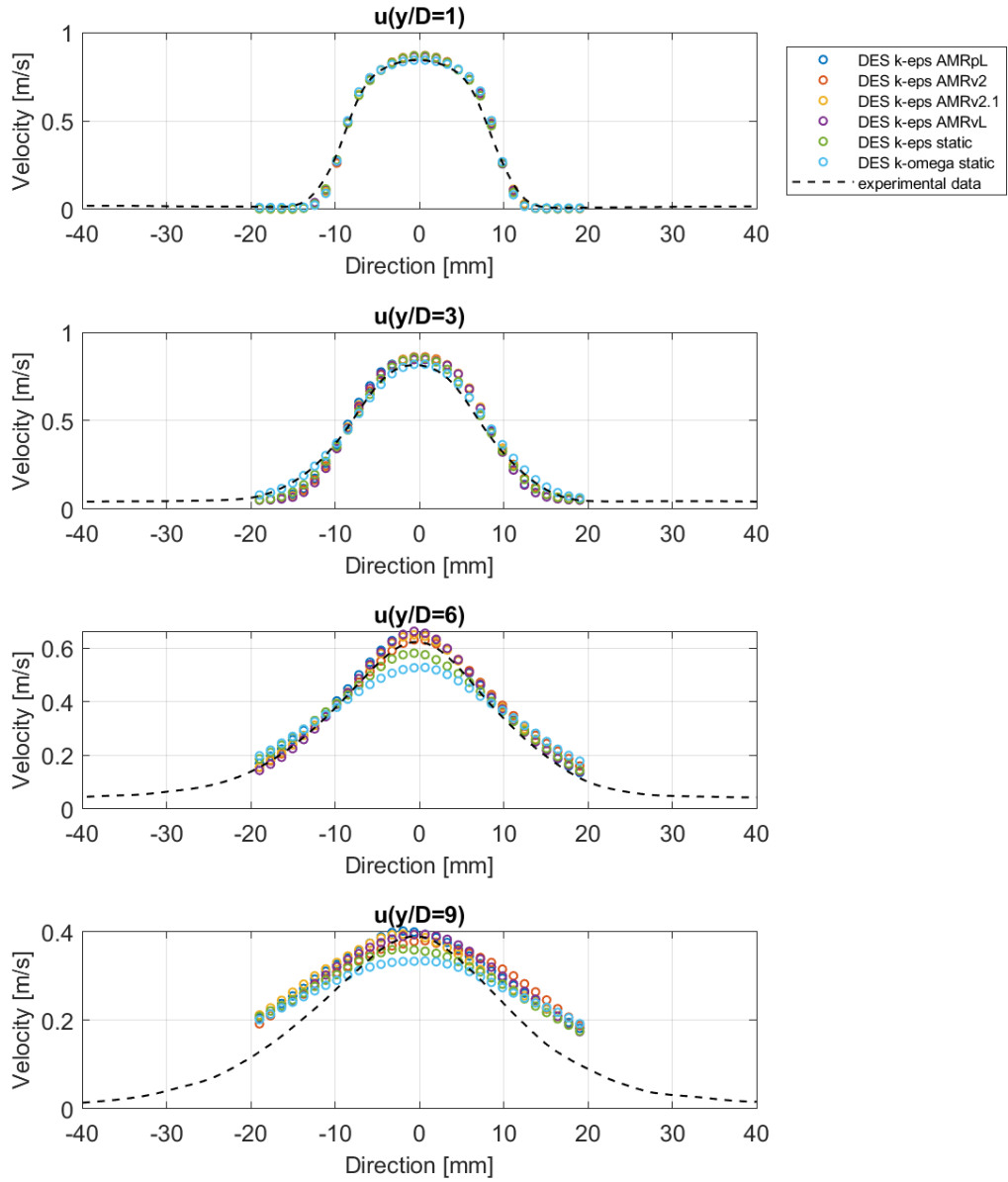


Figure 4.14: Comparison between DES setups velocity mean vertical component at $Y=0$ plane and corresponding experimental data.

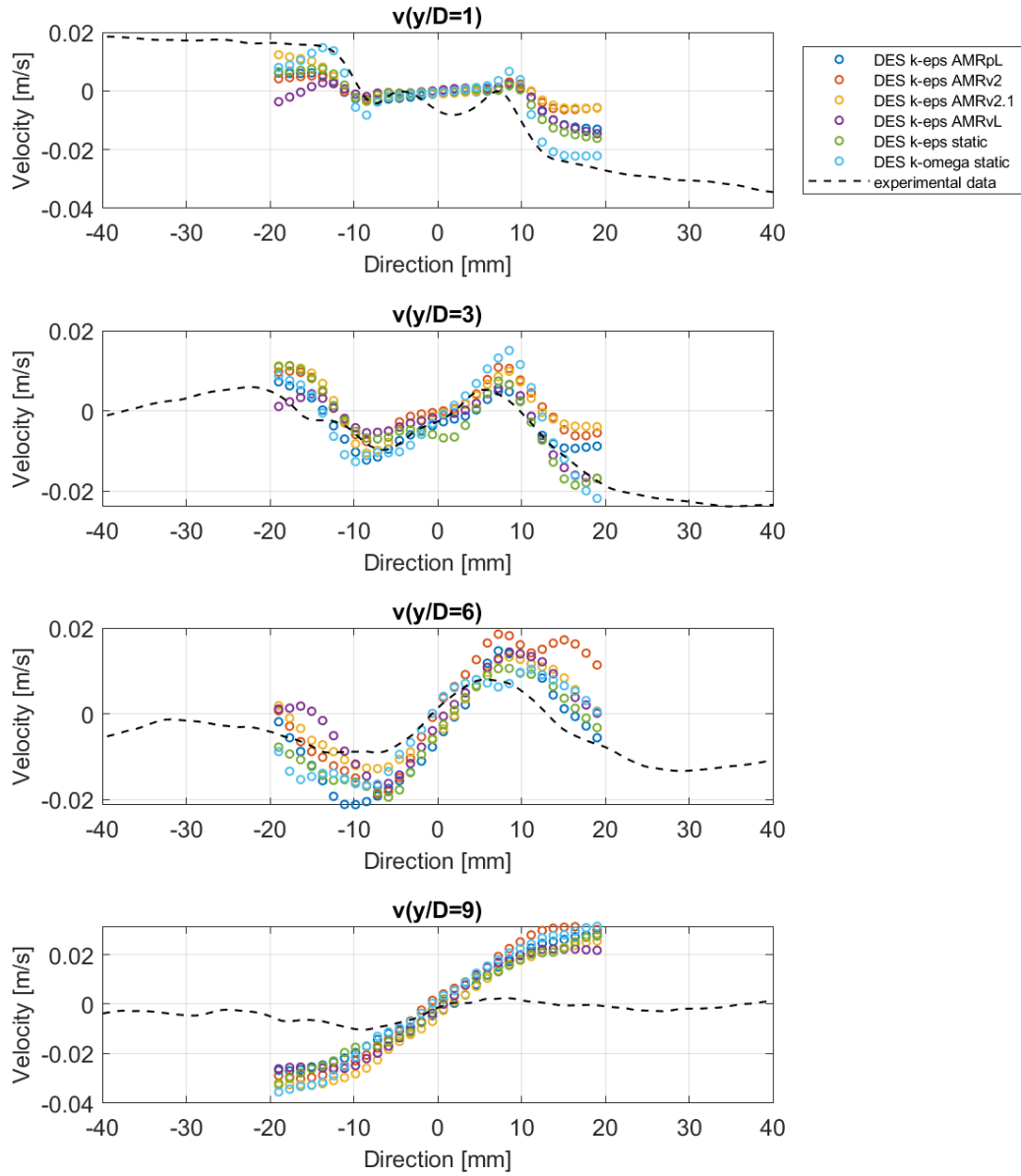


Figure 4.15: Comparison between DES setups velocity mean horizontal component at $Y=0$ plane and corresponding experimental data.

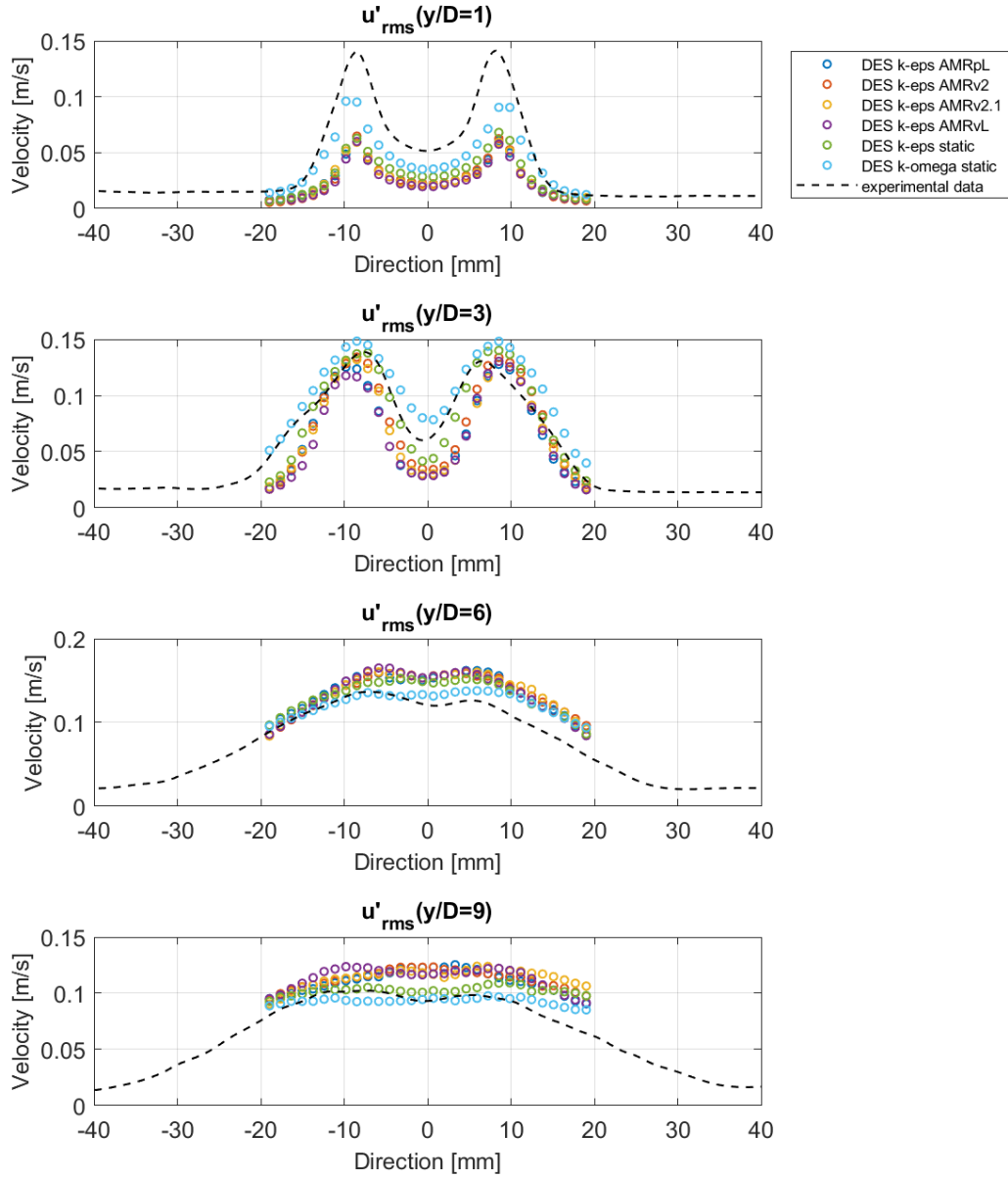


Figure 4.16: Comparison between DES setups root mean squared velocity fluctuation vertical component at $Y=0$ plane and corresponding experimental data.

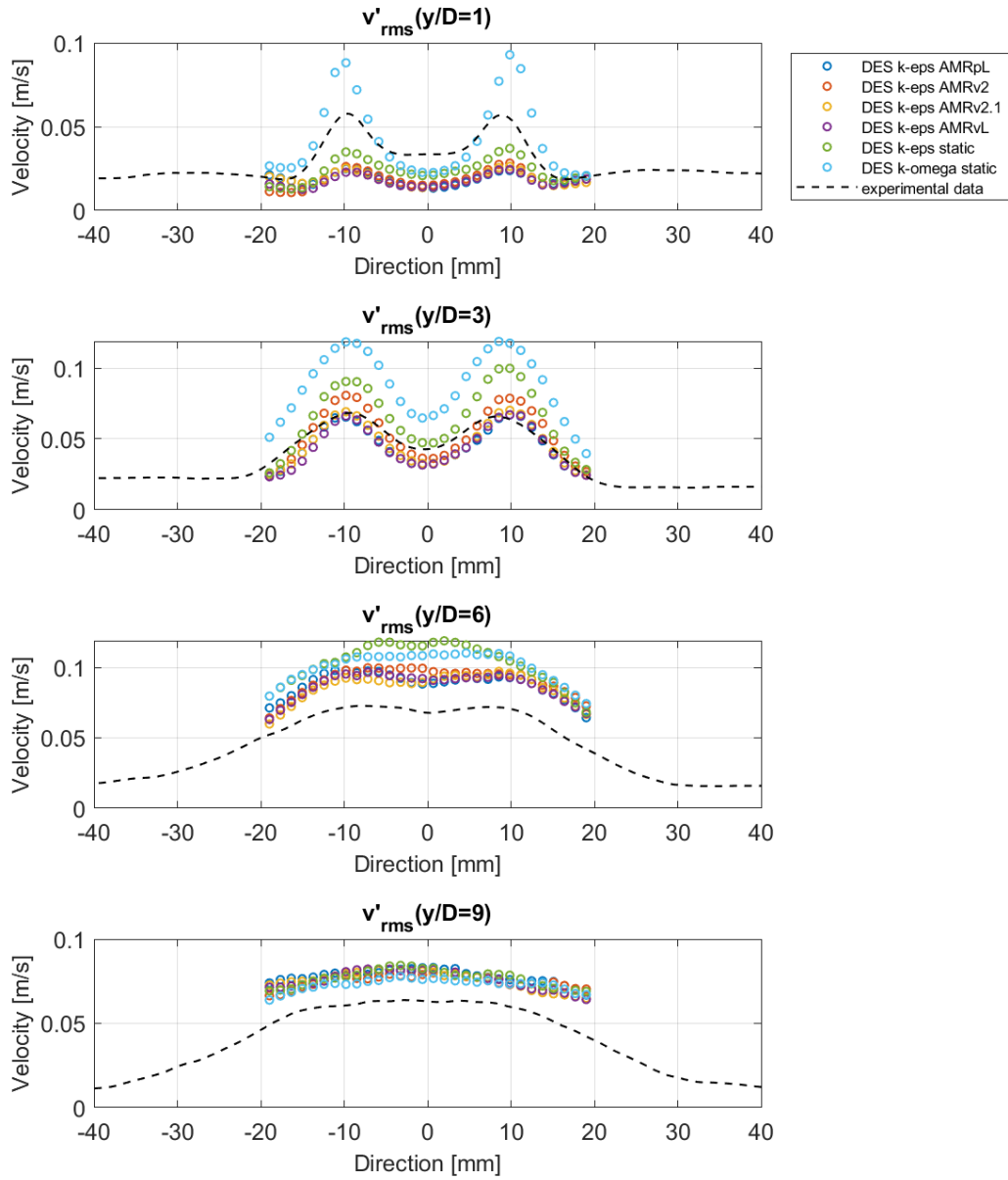


Figure 4.17: Comparison between DES setups root mean squared velocity fluctuation horizontal component at $Y=0$ plane and corresponding experimental data.

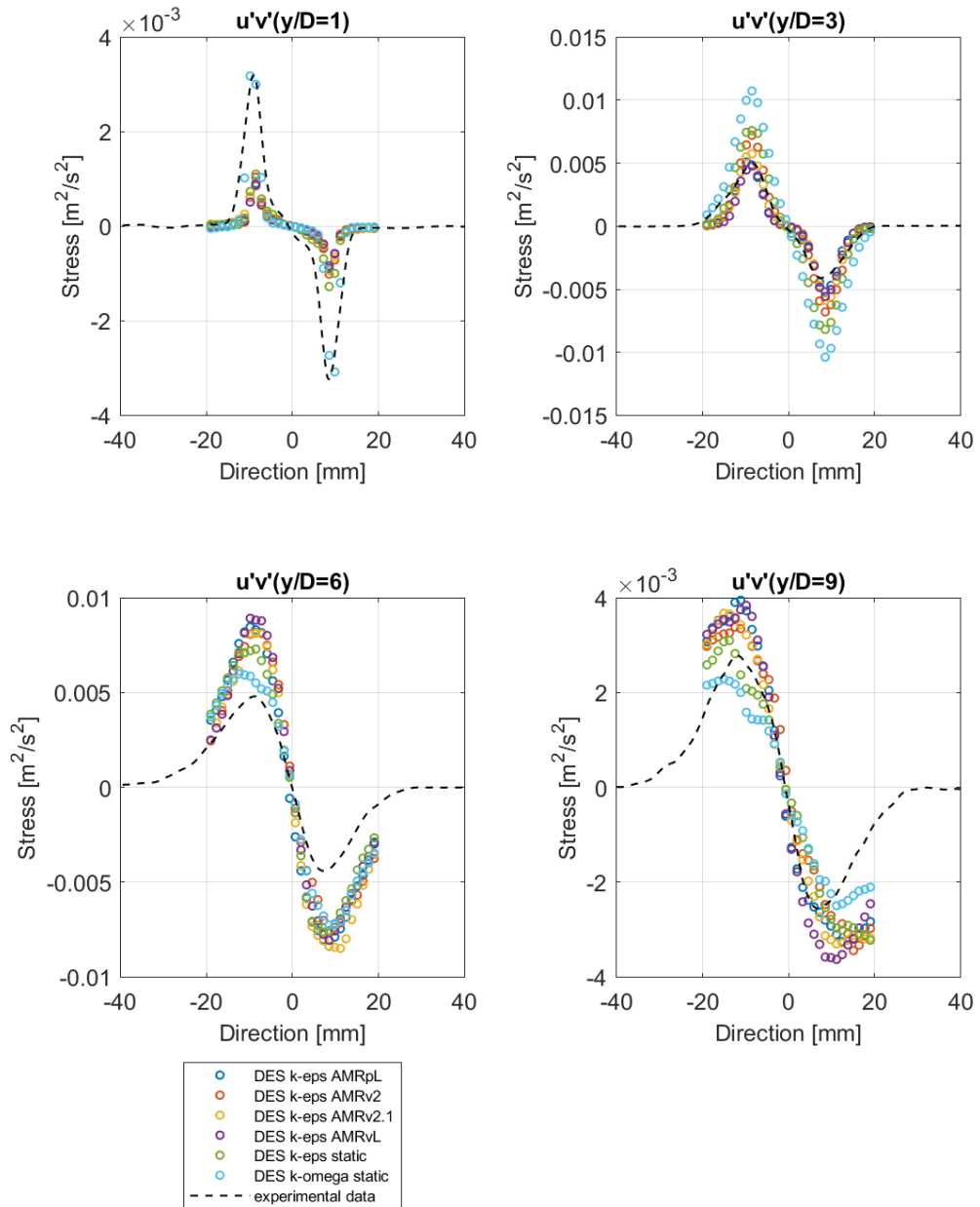


Figure 4.18: Comparison between DES setups of the Reynolds stress $\overline{u'v'}$ at $Y=0$ plane and corresponding experimental data.

Chapter 5

Error estimation

In this chapter, all the setups presented in chapters 3 and 4 will be compared: the aim is to provide an objective mean to evaluate each setup's compatibility with the experiments.

To do so, the subsequent relative error definitions were introduced:

$$\epsilon_{rel} = \frac{\overline{|V_{CFD} - V_{exp}|}}{|V_{exp}|_{max}} \quad (5.1)$$

where, V_{CFD} is the velocity profile calculated through a simulation setup at fixed y/D , and V_{exp} is the experimental velocity at the same y/D coordinate. The difference between the two previous velocity profiles is then averaged to obtain a single ϵ_{rel} value for each y/D coordinate.

The denominator represents the maximum absolute value of the same V_{exp} profile used for the numerator: the absolute value was chosen to overcome a possible negative value, especially for horizontal velocity profiles. The quantity ϵ_{rel} was then calculated for all the setup at every y/D , replacing the generic velocity V progressively with the quantities: \bar{u} , \bar{v} , u'_{rms} , v'_{rms} , $\overline{u'v'}$.

The general definition 5.1 then assumes the following five forms, based on the quantity involved.

$$\epsilon_{\bar{u}} = \frac{\overline{|\bar{u}_{CFD} - \bar{u}_{exp}|}}{|\bar{u}_{exp}|_{max}} \quad (5.2)$$

$$\epsilon_{\bar{v}} = \frac{\overline{|\bar{v}_{CFD} - \bar{v}_{exp}|}}{|\bar{v}_{exp}|_{max}} \quad (5.3)$$

$$\epsilon_{u'_{rms}} = \frac{\overline{|u'_{rmsCFD} - u'_{rmsexp}|}}{|u'_{rmsexp}|_{max}} \quad (5.4)$$

$$\epsilon_{v'_{rms}} = \frac{\overline{v'_{rmsCFD} - v'_{rmsexp}}}{|v'_{rmsexp}|_{max}} \quad (5.5)$$

$$\epsilon_{\overline{u'v'}} = \frac{\overline{u'v'_{CFD} - u'v'_{exp}}}{|\overline{u'v'_{exp}}|_{max}} \quad (5.6)$$

Following definitions 5.2, 5.3, 5.4, 5.5, and 5.6 it is possible to calculate five errors for each setup for a single y/D coordinate. Changing, then, y/D it is possible to evaluate how the error (for a specific quantity) changes in a different part of the domain. The same procedure could be repeated considering a different plane in which the solution was calculated.

The complete set of results is reported in figures 5.1 and 5.2 located at the end of this chapter. These representations confirm what was already observed in chapter 4.

The mean vertical velocity component \bar{v} is captured with relatively high accuracy regardless of the considered y/D . Moreover, the error relative to \bar{v} is lower than 0.2 for all the presented setups.

The same statement could be made considering the errors relative to the root mean square of the vertical fluctuation v'_{rms} : all the DES setups report an error lower than 0.2 at every y/D .

The analysis of the mean horizontal component \bar{v} , however, reveals that the committed error increases drastically at higher y/D : the peak values are comprised between approximately 1.0 and 1.5 and are located at $y/D = 9$. Here, all the setups show a significant difference in the calculated horizontal velocity profile as reported in figures 3.5, 4.10, and 4.15.

In contrast to what was observed for the \bar{v} component, the v'_{rms} errors remain below 0.5 despite the slight increase at higher y/D .

Finally, the stress $\overline{u'v'}$ relative error follows a trend similar to the one observed for v'_{rms} since, of course, it depends on both fluctuation components u' and v' .

Overall, the simulations' match quality decreases as the axial coordinate increases: the critical points are located especially at $y/D = 6$ where the jet flow starts to break into multiple vortexes, and at $y/D = 9$ where the jet flow approaches the upper wall. In the last-mentioned area, the pressure gradients rise and the geometry of the wall forces the jet flow into decelerating and unfolding, so a finer mesh might be required to capture the physical phenomena. This could also explain why the AMRpL setup error relative to the \bar{v} component is the lowest among the DES setups.

By averaging the relative errors at $Z=0$ it is possible to have a clearer view of the overall accuracy of all the setups. The result of this operation is shown in figure

5.3.

By looking at the bar plot, it is then possible to conclude that all the setups have:

- $\overline{\epsilon_{\bar{u}}} \leq 0.1$
- $\overline{\epsilon_{\bar{v}}} < 0.7$
- $\overline{\epsilon_{u'_{rms}}} \leq 0.2$
- $\overline{\epsilon_{v'_{rms}}} \lesssim 0.3$
- $\overline{\epsilon_{u'v'}} \approx 0.3$

The main difference can be observed when comparing the DES setups against the URANS setups, specifically concerning the analysis of the \bar{v} mean relative error: a better prediction can be obtained with the URANS simulations, however, the major drawback is that the velocity fluctuations, and so the stress, cannot be calculated since only the mean flow field is modeled.

Focusing on only the DES setups in figure 5.3, the highest variations concern the \bar{v} relative error: this means that the \bar{v} component might be sensitive to mesh changes as well to the time window selected for the averaging procedure.

The other quantities show lower sensitivity to the selected setup and the error values can be considered more acceptable.

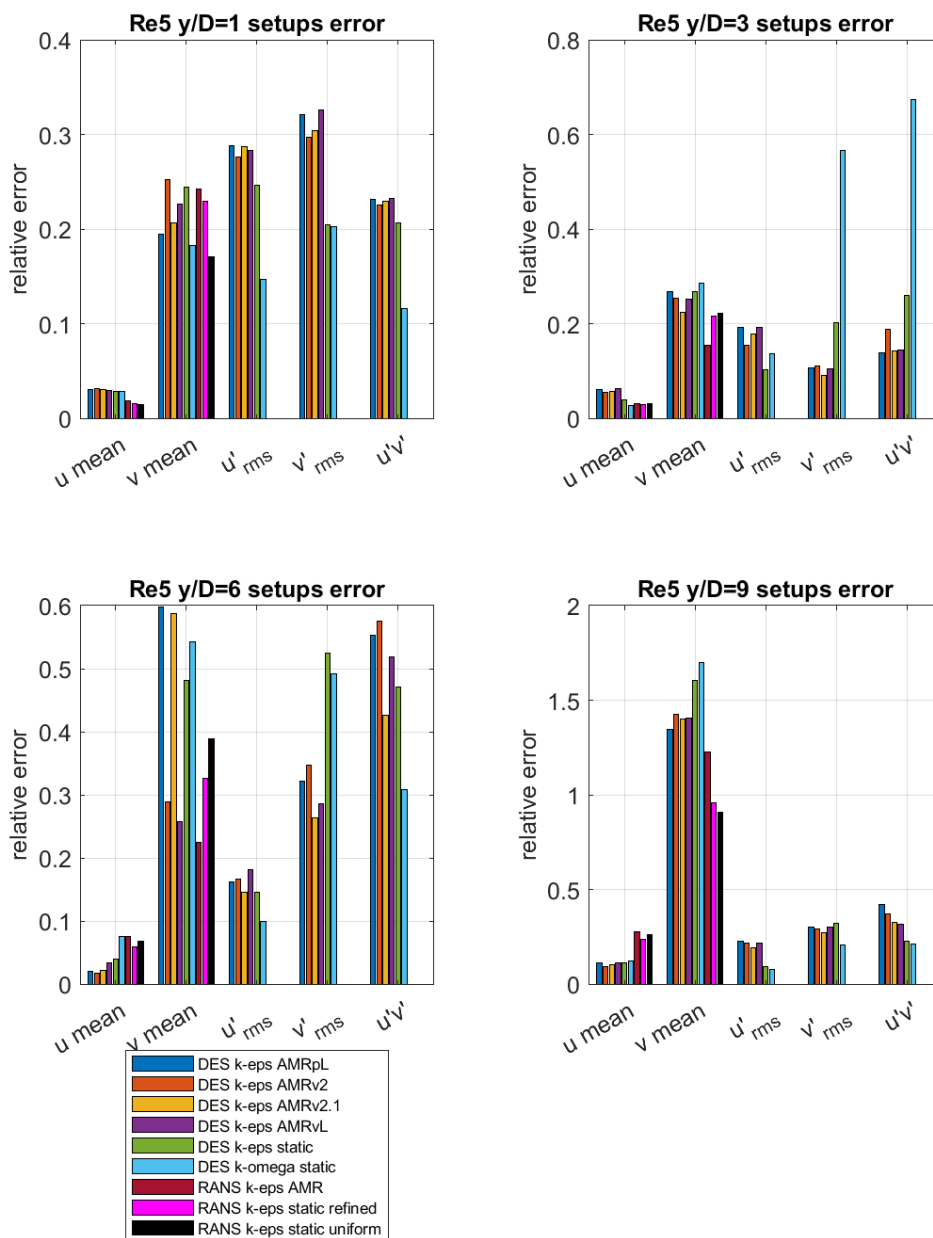


Figure 5.1: Re5 setups comparison through the relative error representation at the Z=0 plane.

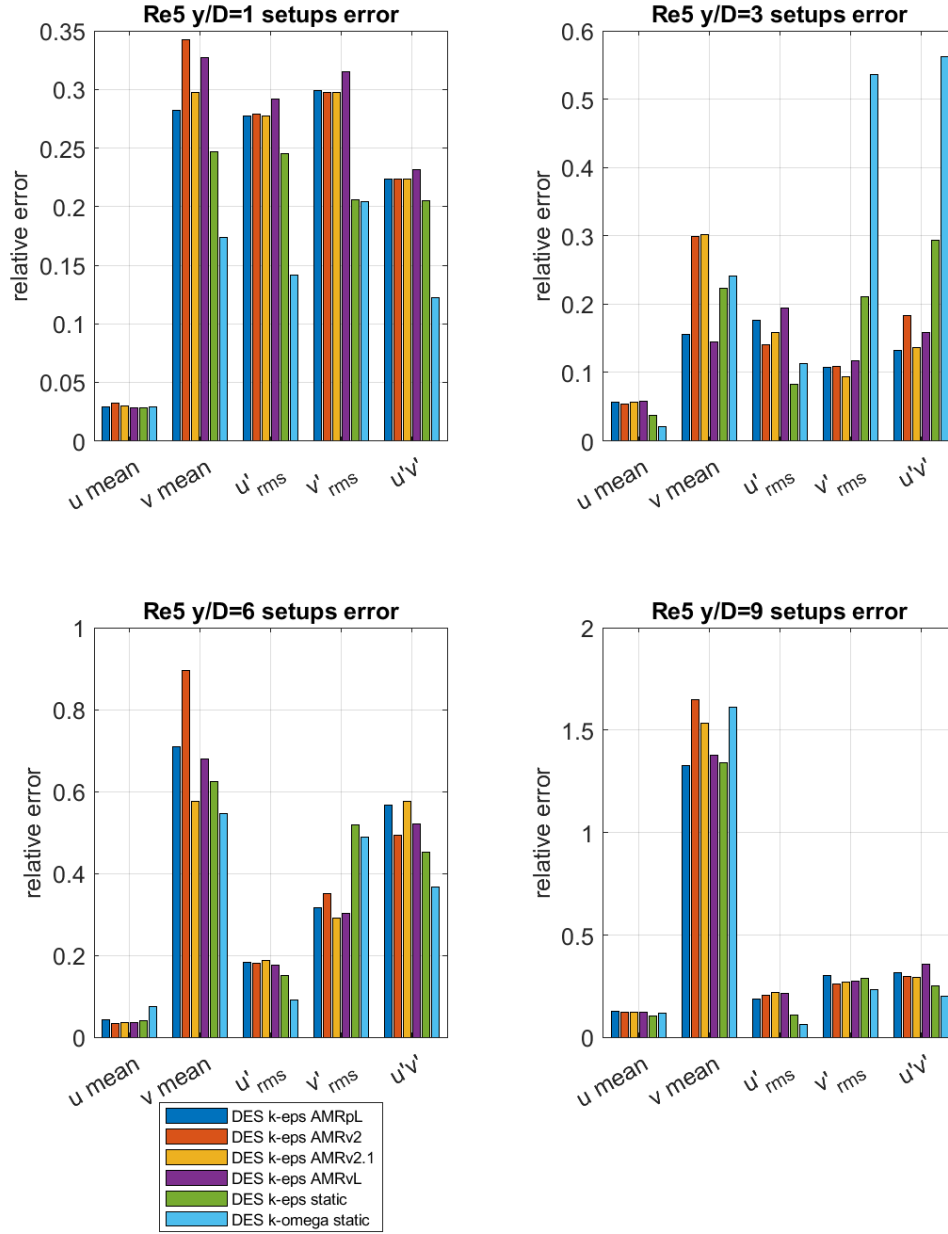


Figure 5.2: Re5 setups comparison through the relative error representation at the $Y=0$ plane.

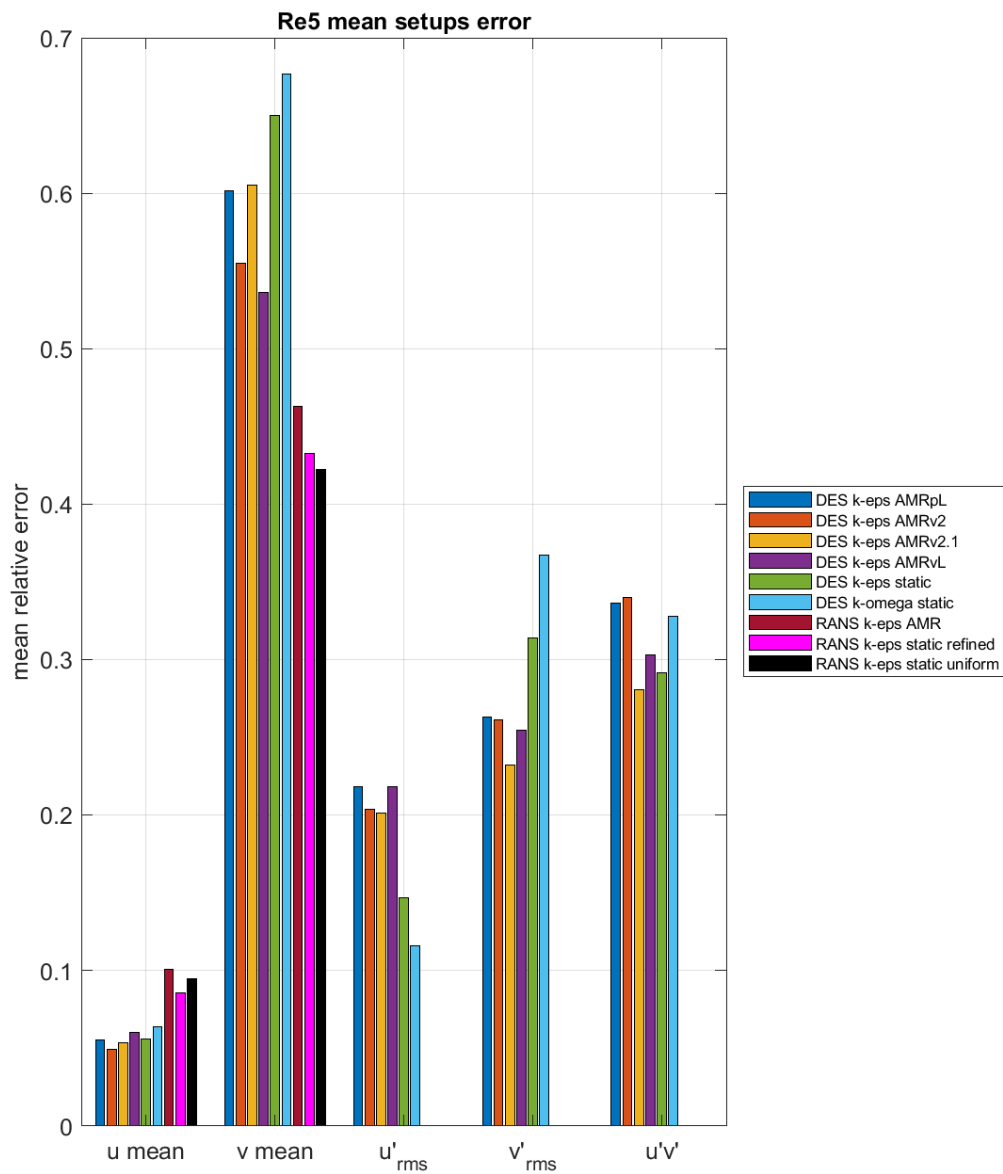


Figure 5.3: Re5 setups comparison through the mean relative error representation at the $Z=0$ plane.

Chapter 6

Conclusions and perspective

At the end of this analysis, a good quality match with the experimental results has been reached throughout the definition of a total of 9 different simulation setups. All the described setups led to a consistent solution: the URANS approach worked as a basis for the DES one, as it was much lighter than the latter. Each URANS simulation provided the set of results in about 24 hours of real-time, however only the mean velocity components results can be utilized for the URANS approach validation. For this reason, URANS simulations could be considered the first computationally affordable method to extract jet mean flow field data in a relatively short amount of time. More computational resources are needed for the DES setups: the set of results, described in chapters 4 and 5, were obtained after approximately 4 weeks of elapsed real time per simulation. Both URANS and DES approaches were run using 24 cores on the CPU nodes of the Legion HPC at Politecnico di Torino (<https://hpc.polito.it/>). However, the use of GPU computational node, allowed in version 2022.1 of STAR-CCM+, reduces significantly the elapsed real-time to just 3 days. The main drawback is that the AMR solver can be run using only CPU nodes in the current version of the software, so only static mesh setups have been simulated using the GPU partition.

The key feature of the AMR model becomes relevant when optimizing the use of computational resources available in the CPU node: the active refinement based on a physical quantity space variation in an unsteady simulation allows to concentrate the grid elements within specific regions. This physics-based refinement can change over time avoiding the lacking of physical accuracy, while possibly reducing the overall cell count. Figures 5.1 and 5.3 showed, in fact, that a good consistency within each setup physical solution has been kept, despite the AMR behaviour. The major improvement was in the required total of number cells, which could be ideally reduced up to $2 \cdot 10^6$.

The most important encountered issue concerns the \bar{v} component: all the simulations reported a significant error that increases as y/D increases. This is a common

issue in all the presented simulations, and the solution will be surely investigated in the future. However, a possible solution could be investigated within the mesh size for $y/D \geq 6$ by slightly modifying the AMR function "keep" range. The mesh size reduction could ultimately affect the Convective Courant Number, so perhaps an Adaptive Time-stepping model could be coupled with the AMR solver to avoid the high-pass filter effect.

The reduction of u'_{rms} and v'_{rms} errors will be another key point of future improvements: the starting point lies in the investigation of the sampling frequency effects on the root mean squared values of the velocity components. The current 50 Hz frequency will be increased up to 2000 Hz to achieve a good representation of the turbulence spectrum up to 1000 Hz. However, this modification will increase the needed post-processing time and the data extraction must be monitored to avoid buffer overloading.

Also, the domain geometry's influence on the solution will be studied. Specifically, this thesis could be expanded with the analysis of the effects that the outlet and inlet surface distances have on the final solution: one possible subsequent study will prove if a more distant inlet surface will affect the jet flow at low y/D and if a faraway outlet surface will change near-impingement field. After all these investigations are complete, the next step could be the implementation of the CFD algorithm for a non-isothermal case, changing the boundary conditions and the physics models accordingly.

In summarising, through the implementation of the AMR model, multiple setups showed a promising consistency with the reality captured by the experimental data provided. Throughout this thesis, it was demonstrated that the match between 2D TR-PIV tests and CFD simulations can be further improved in the future, so the overall analysis described so far can be considered a first valid step towards a more complete computational tool for nuclear systems' design and review.

Appendix A

Periodic simulation for inlet boundary conditions

The so-called periodic simulation takes its name from the wall interface used within its physical domain: a periodic fully-developed interface.

This kind of simulation is an auxiliary computational tool needed to introduce specific inlet boundary conditions that reproduce a fully developed channel flow. Considering the experimental \bar{u} profile at $y/D = 1$ and the HGTR facility representation in figure 1.1, it is possible to deduce that the length of the inflow channel is enough to inject a parabolic velocity distribution within the upper plenum domain. The use of the default velocity inlet boundary condition would have created a uniform distribution of wall-normal velocity equal to V_{avg} . The resulting distribution would have led to a misrepresentation of the entire jet flow field. The most efficient way in terms of required computational resources is to run a relatively light simulation of a small section of the inflow channel using a fully-developed periodic interface. The data needed for the inlet boundary of the upper plenum simulation are collected at the interface of the periodic simulation.

A.1 Computational domain definition

The geometry domain is quite simple: it consists of a cylinder aligned with the x -axis. The circular cross-section corresponds to the upper plenum inlet surface and the length is approximately 5 diameters. The resulting geometry of the pipe and the key boundaries are shown in figure A.1.

Proper boundary conditions were assigned to each surface and reported in table A.1. The flow periodicity can be reproduced creating a periodic fully-developed interface between the inlet and the outlet surfaces and by assigning a target mass flow derived from the experimental data available in table 1.1. For example, at

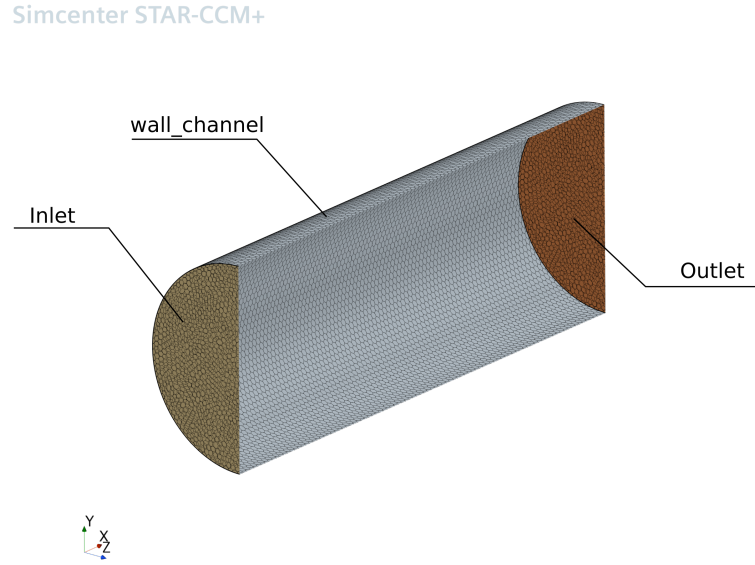


Figure A.1: Inflow pipe geometry representation used for the periodic simulation.

Re5 the entered mass flow is 0.19 kg/s .

Inlet	Mass flow Inlet
Outlet	Pressure Outlet
wall_channel	Wall no slip

Table A.1: Boundary conditions for the periodic simulation.

After the interface definition, the mesh can be generated to obtain a conformal mesh at both the inlet and the outlet. The physics models used for the periodic simulation are equal to the ones used for the upper plenum simulation: however, RANS equations are used despite the model adopted in the upper plenum simulation, whether it is DES or RANS. The fluctuating component of the velocity field is introduced in the upper plenum domain through the synthetic condition when the DES or LES models are used. The addition of this condition allows the use of only RANS equations for the periodic summation, thus reducing the computational resources needed. On the other hand, the turbulence model should be changed according to the one used in the upper plenum simulation to gather proper boundary data from the periodic simulation.

Simcenter STAR-CCM+

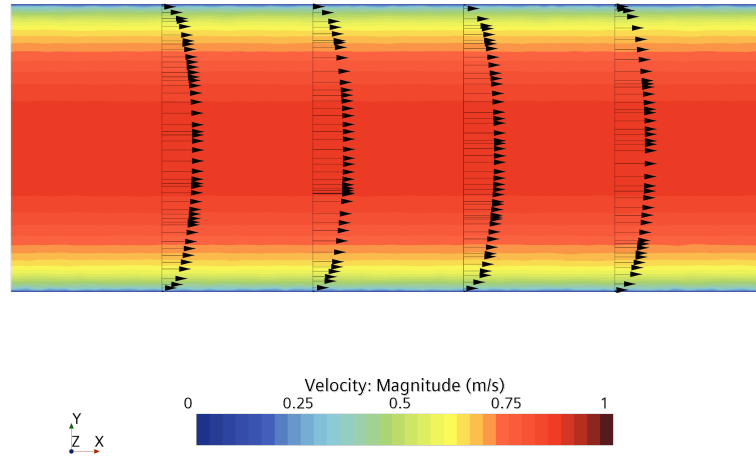


Figure A.2: Inflow pipe velocity scalar field at $Z=0$ plane in addition to the representation of the axial velocity profile at 4 different cross-section planes.

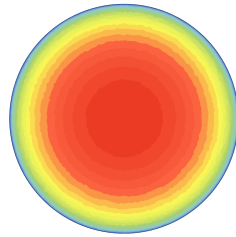
A.2 Boundary physics values needed

After the periodic simulation has been run for the right amount of iterations, the solution at one interface (both inlet and outlet interfaces are equivalent in terms of physical quantities thanks to the imposed periodicity) can be exported in comma separated values files to be used in other simulations.

The overall solution in terms of velocity is displayed in figure A.2. The latter representation shows also the parabolic axial velocity typical of a fully developed channel flow.

Figure A.3 shows part of the results at the periodic interface needed for upper plenum simulations, however, other quantities like specific dissipation rate (for $\kappa - \omega$ model), turbulent dissipation rate (for $\kappa - \epsilon$), or turbulent length scale (for DES synthetic conditions), can also be provided to upper plenum simulations.

Simcenter STAR-CCM+

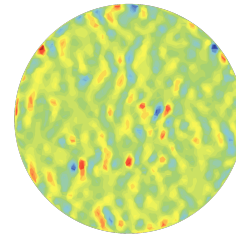


Z
Y X

Velocity[i] (m/s)
0 0.25 0.5 0.75 1

(a) Velocity component along the x axis at the periodic interface

Simcenter STAR-CCM+

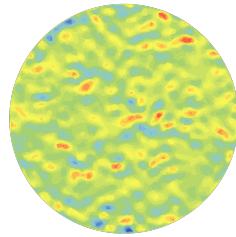


Z
Y X

Velocity[j] (m/s)
-0.004 -0.002 0 0.002 0.004

(b) Velocity component along the y axis at the periodic interface

Simcenter STAR-CCM+

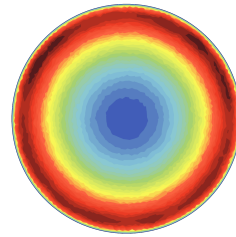


Z
Y X

Velocity[k] (m/s)
-0.004 -0.002 0 0.002 0.004

(c) Velocity component along the z axis at the periodic interface

Simcenter STAR-CCM+



Z
Y X

Turbulent Kinetic Energy (J/kg)
0 0.0015 0.003 0.0045 0.006

(d) Turbulent kinetic energy at the periodic interface

Figure A.3: Scalar scenes of velocity components and turbulent kinetic energy at the periodic interface.

Appendix B

Preliminary jet oscillation study

The total physical time required by URANS simulations was estimated thanks to a preliminary jet oscillation study done on a Re5 static mesh configuration.

This study concerns the time monitoring of the peak velocity position at two different plenum cross-sections. Specifically, the space coordinates of the maximum vertical velocity were represented through time at $x/D = 6$ and $x/D = 9$ planes¹. Then, the resulting data were interpolated using a sine fitting with a 95% target of confidence bounds. The general sine function used for the interpolation is reported as follows:

$$f(t) = a_1 \cdot \sin(b_1 \cdot t + c_1) \quad (\text{B.1})$$

The coordinates data and the interpolating function are reported in figure B.1. The a_1 , b_1 , and c_1 coefficients obtained after the interpolation are reported in table B.1. Noting that the b_1 coefficient represents the oscillation velocity in rad/s , the period can be calculated using the subsequent definition:

$$T = \frac{2\pi}{b_1} \quad (\text{B.2})$$

The calculated oscillation time periods are also reported in table B.1.

By looking at the reported result, the best compromise between computational cost and steady-state achievement was determined at a total simulation time of approximately 20 seconds. This resulting time period was used as a reference for Re5 URANS setups time discretization.

¹The plane denomination refers to the actual computational domain coordinate system

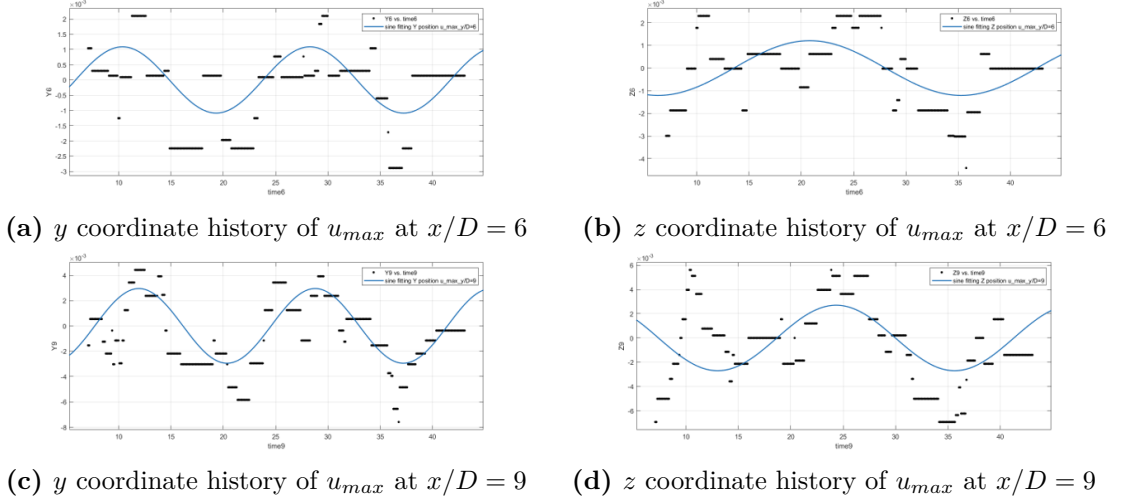


Figure B.1: Space coordinates of the maximum vertical velocity through time at $y/D = 6$ and $y/D = 9$ planes, in addition with the sine interpolation plot. The position unit is meters, and time is expressed in seconds.

	Y6	Z6	Y9	Z9
a_1	0.001087	0.001209	0.002952	0.002697
b_1	0.3506	0.2168	0.3726	0.2778
c_1	-2.061	-2.939	-2.872	1.092
T	17.91	28.97	16.85	22.61

Table B.1: Fitting coefficient calculated after sine interpolation.

Bibliography

- [Eng21] American Society of Engineers. «ASME V&V 2021 Virtual, Online Verification Validation Symposium, May 19 - 20, 2021». In: (2021). URL: <https://event.asme.org/VandV-2021/Program/Challenge-Problems> (cit. on p. 1).
- [Sie21] Siemens. «Simcenter STAR-CCM+ product overview». In: (2021). URL: <https://www.plm.automation.siemens.com/global/en/products/simcenter/STAR-CCM.html> (cit. on p. 10).
- [Alw+19] Anas Alwafi, Thien Nguyen, Yassin Hassan, and N.K. Anand. «Time-resolved particle image velocimetry measurements of a single impinging jet in the upper plenum of a scaled facility of high temperature gas-cooled reactors». In: *International Journal of Heat and Fluid Flow* 76 (2019), pp. 113–129. ISSN: 0142-727X. DOI: <https://doi.org/10.1016/j.ijheatfluidflow.2019.02.003>. URL: <https://www.sciencedirect.com/science/article/pii/S0142727X1830715X> (cit. on pp. 3–6).
- [McV+15] Kyle L. McVay, Jae-Hyung Park, Saya Lee, Yassin A. Hassan, and N.K. Anand. «Preliminary tests of particle image velocimetry for the upper plenum of a scaled model of a very high temperature gas cooled reactor». In: *Progress in Nuclear Energy* 83 (2015), pp. 305–317. ISSN: 0149-1970. DOI: <https://doi.org/10.1016/j.pnucene.2015.04.004>. URL: <https://www.sciencedirect.com/science/article/pii/S014919701500092X> (cit. on p. 2).
- [MH10] *PIV Study of the Near-Field Region of a Turbulent Round Jet*. Vol. ASME 2010 3rd Joint US-European Fluids Engineering Summer Meeting: Volume 1, Symposia – Parts A, B, and C. Fluids Engineering Division Summer Meeting. Aug. 2010, pp. 1353–1361. DOI: 10.1115/FEDSM-ICNMM2010-31139. eprint: https://asmedigitalcollection.asme.org/FEDSM/proceedings-pdf/FEDSM2010/49484/1353/4591185/1353_1.pdf. URL: <https://doi.org/10.1115/FEDSM-ICNMM2010-31139> (cit. on p. 6).

- [FBP09] H. Fellouah, C.G. Ball, and A. Pollard. «Reynolds number effects within the development region of a turbulent round free jet». In: *International Journal of Heat and Mass Transfer* 52.17 (2009). Special Issue Honoring Professor D. Brian Spalding, pp. 3943–3954. ISSN: 0017-9310. DOI: <https://doi.org/10.1016/j.ijheatmasstransfer.2009.03.029>. URL: <https://www.sciencedirect.com/science/article/pii/S0017931009002063> (cit. on p. 6).
- [PS07] International Association for the Properties of Water and Steam. «Revised Release on the IAPWS Industrial Formulation 1997 for the Thermodynamic Properties of Water and Steam, IAPWS Secretariat, Lucerne, Switzerland». In: (2007). URL: www.iapws.org (cit. on p. 9).
- [Jar+06] N. Jarrin, S. Benhamadouche, D. Laurence, and R. Prosser. «A synthetic eddy-method for generating inflow conditions for large-eddy simulations». In: *International Journal of Heat and Fluid Flow* 27.4 (2006). Special Issue of The Fourth International Symposium on Turbulence and Shear Flow Phenomena - 2005, pp. 585–593. ISSN: 0142-727X. DOI: <https://doi.org/10.1016/j.ijheatfluidflow.2006.02.006>. URL: <https://www.sciencedirect.com/science/article/pii/S0142727X06000282> (cit. on p. 21).
- [MC06] Glenn E McCreery and Keith G Condie. *Experimental modeling of VHTR plenum flows during normal operation and pressurized conduction cooldown*. Tech. rep. Idaho National Lab.(INL), Idaho Falls, ID (United States), 2006 (cit. on p. 1).
- [03] «A Technology Roadmap for Generation IV Nuclear Energy Systems Executive Summary». In: (Mar. 2003). DOI: 10.2172/859105. URL: <https://www.osti.gov/biblio/859105> (cit. on p. 2).